

# p65 signaling dynamics drive the developmental progression of hematopoietic stem and progenitor cells through cell cycle regulation

Received: 18 January 2024

Accepted: 20 August 2024

Published online: 06 September 2024


 Check for updates

Clyde A. Campbell<sup>1</sup>  , Rodolfo Calderon<sup>1</sup>, Giulia Pavani<sup>2</sup>, Xiaoyi Cheng<sup>1</sup>, Radwa Barakat<sup>1,3</sup>, Elizabeth Snella<sup>1</sup>, Fang Liu<sup>1</sup>, Xiyu Peng<sup>4</sup>, Jeffrey J. Essner<sup>1</sup>, Karin S. Dorman<sup>1,4</sup>, Maura McGrail<sup>1</sup>, Paul Gadue<sup>2</sup>, Deborah L. French<sup>2</sup> & Raquel Espin-Palazon<sup>1</sup>  

Most gene functions have been discovered through phenotypic observations under loss of function experiments that lack temporal control. However, cell signaling relies on limited transcriptional effectors, having to be re-used temporally and spatially within the organism. Despite that, the dynamic nature of signaling pathways have been overlooked due to the difficulty on their assessment, resulting in important bottlenecks. Here, we have utilized the rapid and synchronized developmental transitions occurring within the zebrafish embryo, in conjunction with custom NF- $\kappa$ B reporter embryos driving destabilized fluorophores that report signaling dynamics in real time. We reveal that NF- $\kappa$ B signaling works as a clock that controls the developmental progression of hematopoietic stem and progenitor cells (HSPCs) by two p65 activity waves that inhibit cell cycle. Temporal disruption of each wave results in contrasting phenotypic outcomes: loss of HSPCs due to impaired specification versus proliferative expansion and failure to delaminate from their niche. We also show functional conservation during human hematopoietic development using iPSC models. Our work identifies p65 as a previously unrecognized contributor to cell cycle regulation, revealing why and when pro-inflammatory signaling is required during HSPC development. It highlights the importance of considering and leveraging cell signaling as a temporally dynamic entity.

Hematopoietic stem and progenitor cells (HSPCs) are multipotent, self-renewing cells that maintain the blood system throughout the life of all vertebrates. The unique properties of these cells make HSPC transplantation an effective therapy for the treatment of many blood disorders. However, the insufficient number of bone marrow donors,

the rarity of engraftable HSPCs, and complications including graft-versus-host disease have led to a search for alternative sources of HSPCs. The advent of induced-pluripotent stem cells (iPSCs) led to great optimism in the field as a potentially limitless source of immunologically-matched hematopoietic cells and their derivatives<sup>1</sup>.

<sup>1</sup>Department of Genetics, Development and Cell Biology; Iowa State University, Ames, IA 50011, USA. <sup>2</sup>Center for Cellular and Molecular Therapeutics, The Children's Hospital of Philadelphia, Philadelphia, PA, USA. <sup>3</sup>Department of Toxicology, Faculty of Veterinary Medicine, Benha University, Qalyubia 13518, Egypt. <sup>4</sup>Department of Statistics, Iowa State University, Ames, IA 50011, USA.  e-mail: [clyde@iastate.edu](mailto:clyde@iastate.edu); [espin@iastate.edu](mailto:espin@iastate.edu)

During the last two decades, numerous laboratories have identified a plethora of signaling pathways, growth factors, transcription factors, and morphogens fundamental to drive HSPC specification, which occurs once in an organism's lifetime during embryonic development. These include: WNT<sup>2–5</sup>, Notch<sup>6</sup>, HIF<sup>7,8</sup>, TGFB<sup>9</sup>, retinoic acid<sup>10</sup>, HOXA<sup>11</sup>, FGF<sup>12</sup>, BMP<sup>13</sup>, VEGF<sup>14</sup>, RUNX1<sup>15</sup>, GATA2<sup>16–18</sup>, GFII<sup>19</sup>, GATA3<sup>20</sup>, MEIS1<sup>21</sup>, and inflammatory signaling<sup>22–25</sup>, among others. These molecular drivers of HSPC fate have been identified mostly by loss of function experiments that lacked temporal control. However, resolving their temporal requirements, which is the objective of this study, is key for their application into in vitro cultures to successfully derive human HSPCs. Only recently it has been reported the production of serially transplantable HSPCs from human iPSCs<sup>26</sup>. However, this protocol relied on embryonic bodies, and therefore the complex interaction and signals among the mixture of cell types co-developing with low numbers of hemogenic endothelium, challenging to identify. Having an in-depth understanding of the temporally and spatially orchestrated natural molecular network that drives HSPC specification will undoubtedly improve current in vitro protocols of human hematopoietic differentiation, increasing the yield of these rare hemogenic endothelium events to successfully develop future HSPC-based protocols for human disease modeling and perhaps clinical immunotherapies and transfusions from its derivatives.

HSPCs arise from the major arteries of the embryo through the transdifferentiation of a subset of endothelial cells (ECs), designated hemogenic endothelium (HE), into pre-HSPCs and their subsequent maturation into functional HSPCs<sup>27–31</sup>. HSPC specification is highly conserved among vertebrates<sup>32</sup>, requiring the silencing of endothelial-specific genes and expression of hematopoietic master regulators such as *runx1*, *cmyb*, and *gata2*, a process named endothelial to hematopoietic transition (EHT)<sup>33</sup>. EHT occurs between E8.5–11.5 in the mouse<sup>29,34</sup>, and 24–52 hpf in the zebrafish embryo<sup>35–37</sup>. Although the main EHT drivers have been characterized, the molecular mechanisms that prime ECs prior to EHT to becoming hemogenic (E5.5–E8.5 in mouse<sup>38,39</sup>; 16–24 hpf in zebrafish embryo<sup>40</sup>) and their temporal dynamics are poorly understood. This is due to (i) the lack of specific markers that differentiate ECs from those that will acquire hemogenic potential; (ii) the difficulty of experimenting with mammalian embryos in the early stages of development; and (iii) the slow mammalian embryonic development that dampens the identification of signaling dynamics across time. Understanding how ECs are primed to undergo a hemogenic switch through the identification of a robust marker that segregates ECs with hemogenic capabilities before they express hematopoietic markers, will be fundamental to correctly program endothelial-like cells in in vitro systems to generate functional HSPCs, as well as for the characterization of these enigmatic ECs. Moreover, understanding the exact temporal dynamics when the main HSPC inducers need to be turned on and off is critical to improve current in vitro protocols. Both of these roadblocks have been overcome in this study.

Current human differentiation protocols have been primarily extrapolated from animal models. Among these, zebrafish (*Danio rerio*), due to their embryonic transparency, high fertility, and conserved hematopoietic system with humans, has facilitated key discoveries in hematopoiesis<sup>41</sup>. Particularly, the advantages offered by the zebrafish model for the in vivo visualization of HSPC development during their external embryonic development while avoiding artificial inflammation occurring through invasive manipulations of the mammalian embryo, enabled us and others to reveal pro-inflammatory signaling as a critical pathway driving HSPC specification<sup>22–25,40,42</sup>. In vivo, several inflammatory mediators such as Tnfa, Il1b, Tlr4, inflammasome, and RIG-I-like receptors converge into NF- $\kappa$ B activation to specify HSPCs<sup>43,44</sup>. Recently, we showed that, in the aseptic embryo, ECs required priming by the microbial sensor Nod1 and NF- $\kappa$ B activation to switch fate towards definitive HE cells, a prerequisite to specify

HSPCs<sup>40</sup>. Interestingly, we found NF- $\kappa$ B activated prior to EHT<sup>40</sup>, while previous studies suggested NF- $\kappa$ B was activated during EHT<sup>25,42</sup>. In all these studies, NF- $\kappa$ B activity was monitored in the dorsal aorta (DA) using double transgenic zebrafish embryos harboring the vascular (*kdr1:mCherry*)<sup>35</sup> and NF- $\kappa$ B (*NF- $\kappa$ B:eGFP*)<sup>45</sup> reporters. This latter contained the human NF- $\kappa$ B recognition sequence (GGAAAGTCCC)<sub>6</sub> driving the expression of eGFP, a protein highly stable with a half-life of >26 h, challenging the temporal identification of NF- $\kappa$ B activity during HSPC development. Resolving the temporal requirement of NF- $\kappa$ B signaling during HSPC development would be critical to leverage this knowledge in vitro for the generation of HSPCs, a knowledge gap that is covered in this work. Moreover, many fundamental questions still remained open concerning how inflammatory signaling specifies HSPCs.

Our work provides unique genetic and chemical tools that uncover several fundamental outstanding questions not only in the hematopoietic stem cell field, but also in the general field of biology. First, through the generation of novel NF- $\kappa$ B embryonic reporter lines, we show that NF- $\kappa$ B activity can be utilized to isolate and characterize ECs with hemogenic capabilities before they undergo EHT and become HECs. Second, we demonstrate that two waves of pro-inflammatory signaling are present during HSPC development, the first during EC induction, and a second wave during the delamination of nascent HSPCs from the aortic niche. Each of these waves, which were p65-dependent, are critical at a specific time during HSPC development to drive two distinct functions that rely on cell cycle control. Last, we reveal that the precise temporal inhibition of p65 during HSPC delamination allowed HSPC proliferation while keeping them in their aortic niche. This knowledge could re-direct efforts to achieve the eluded goal of increasing HSPC yield in in vitro protocols of human hematopoietic differentiation, unlocking their use for disease modeling and future therapies. Importantly, our work demonstrates the importance of considering cell signaling as a temporally dynamic entity that drives differential functional outcomes over time.

## Results

### Real-time NF- $\kappa$ B activity dynamics during HSPC development

Zebrafish HSPC development occurs during embryonic development through the following stages: (1) mesoderm formation; (2) endothelial differentiation/artery fate determination; (3) HE induction; (4) endothelial to hematopoietic (EHT) transition, when hematopoietic markers express; and (5) HSPC release from the DA through endothelial to mesenchymal transition (EndMT)<sup>46</sup> (Fig. 1A).

Because eGFP is very stable (>26 h)<sup>47</sup>, and zebrafish embryonic development is extremely rapid, we hypothesized that the previously published *Tg(NF $\kappa$ B:eGFP)<sup>cl</sup>* reporter line<sup>45</sup> may not faithfully reflect the potential dynamic nature of NF- $\kappa$ B activation. To overcome this challenge, we generated a novel NF- $\kappa$ B zebrafish reporter line—*Tg(6xHsa.NF $\kappa$ B:d2EGFP)<sup>iso2</sup>*, herein called *Tg(NF- $\kappa$ B:d2EGFP)*—by replacing the stable eGFP with a destabilized version (d2EGFP) with a shorter half-life of 2 h<sup>48</sup> (Fig. 1B). *Tg(NF- $\kappa$ B:d2EGFP)* exhibited strong *d2EGFP* expression within regions of known NF- $\kappa$ B activity in the developing embryo<sup>45</sup> (Fig. Sup 1A–D). The previously reported half-life of 2 h of the d2EGFP was validated in vivo incubating *kdr1:mCherry<sup>+</sup>, NF- $\kappa$ B:d2EGFP<sup>+</sup>* embryos from 20–22 hpf with the herein validated NF- $\kappa$ B inhibitor Caffeic acid phenethyl ester (CAPE)<sup>49</sup> (Fig. Sup 2). To quantify the NF- $\kappa$ B signaling dynamics during HSPC development, we performed flow cytometry from *NF- $\kappa$ B:d2EGFP<sup>+</sup>; kdr1:mCherry<sup>+</sup>* embryos starting at 16 h post fertilization (hpf), the time when NF- $\kappa$ B activity was first detected in the primitive vascular cord<sup>40</sup>. As shown in Fig. 1C, NF- $\kappa$ B activity in the endothelium trunk peaked at 22 hpf with ~46% of NF- $\kappa$ B<sup>+</sup> ECs cells; and by 30 hpf, decreased to ~6%. At 34 hpf we observed a reactivation of NF- $\kappa$ B activity within ~15% of ECs, which was subsequently decreased to ~7% at 48 hpf. To visualize if NF- $\kappa$ B activity localized to the blood-forming regions of the DA, we performed live

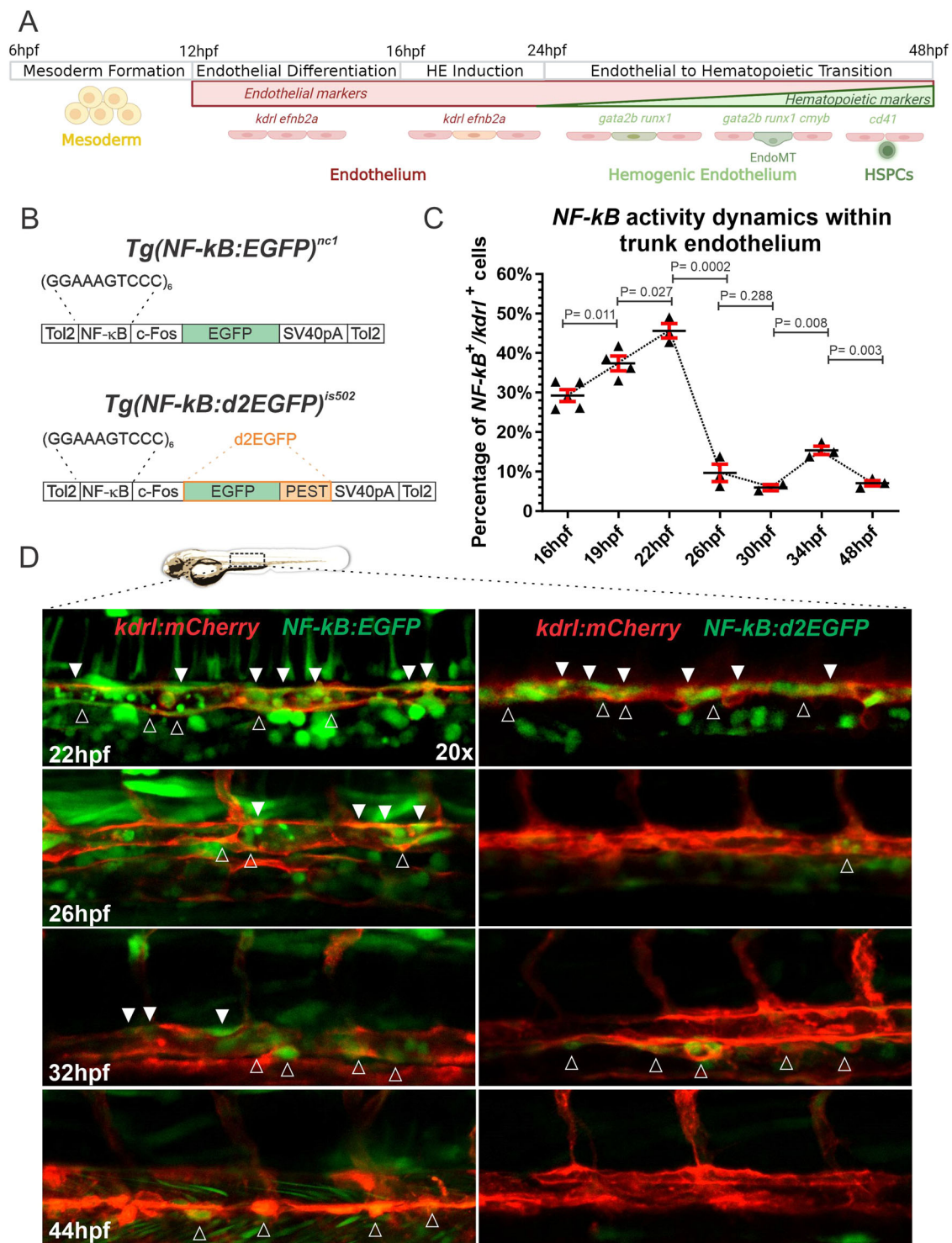


**Fig. 1 | *Tg(NF-κB:d2EGFP)<sup>is502</sup>* embryos reveal real-time NF-κB activation dynamics within the endothelium. A** HSPC development in zebrafish embryos. Mesoderm is specified from 6hpf and endothelial precursors from 12hpf. Hemogenic endothelium (HE) can be visualized within the dorsal aorta by WISH for *runx1* and *gata2b*, and subsequently *cmyb*, from 22–48hpf. Emergent HSPCs can be labeled within the floor of the dorsal aorta from 48hpf with the reporter *Tg(cd41:eGFP)*. **B** Schematic diagrams of constructs used to generate *Tg(NF-κB:EGFP)<sup>nc1</sup>* (top)<sup>45</sup> and *Tg(NF-κB:d2EGFP)<sup>is502</sup>* (bottom) (this work). **C** Flow cytometric quantification of *NF-κB:d2EGFP<sup>+</sup>; kdr1:mCherry<sup>+</sup>* cells within surgically isolated embryonic trunks at 16, 19, 22, 26, 30, 34, and 48hpf. Each dot represents 20–25 pooled embryonic trunks. Black horizontal lines indicate mean ± SD (red). 16hpf

(*n* = 5), 19hpf (*n* = 4), 22hpf (*n* = 3), 26hpf (*n* = 3), 30hpf (*n* = 2), 34hpf (*n* = 3), and 48hpf (*n* = 3). Statistics were generated using an unpaired two-tailed *T*-test. Source data are provided as a Source Data file. **D** Representative 20x maximum projection confocal images of the trunk region of live *NF-κB:EGFP<sup>+</sup>; kdr1:mCherry<sup>+</sup>* (left panels), and *NF-κB:d2EGFP<sup>+</sup>; kdr1:mCherry<sup>+</sup>* (right panels) embryos imaged at 22, 26, 32, and 44hpf. Outlined and solid white arrowheads indicate NF-κB activity within the ventral side or roof, respectively, of the developing vascular cord. Each timepoint was repeated three times independently with similar results. Figure 1A created with BioRender.com released under a Creative Commons Attribution-NonCommercial-NoDerivs 4.0 International license.



confocal imaging starting at the peak of NF- $\kappa$ B activity (22 hpf) (Fig. 1D). While *NF- $\kappa$ B:eGFP* embryos showed sustained NF- $\kappa$ B activity in the developing vascular cord at times evaluated, *Tg(NF- $\kappa$ B:d2EGFP)* reported two distinct NF- $\kappa$ B activation stages (Fig. 1D), agreeing with the data shown in Fig. 1C. At 22 hpf, both reporter lines revealed NF- $\kappa$ B<sup>+</sup> cells in vascular cord. At 32 hpf, NF- $\kappa$ B<sup>+</sup> cells were restricted to the aortic floor (outlined arrowheads) only in the *NF- $\kappa$ B:d2EGFP* reporter line, showing initial detachment from the aortic niche, a characteristic feature of emerging HSPCs<sup>35,36,50</sup>. These results demonstrate that during HSPC development, NF- $\kappa$ B signaling activates intrinsically within two distinct waves (16–24 hpf and 32–44 hpf).

### NF- $\kappa$ B<sup>+</sup> endothelium displays hallmarks of quiescence and upregulated p65

Although NF- $\kappa$ B signaling was identified as a critical inductor of HSPC fate a decade ago<sup>25</sup>, it is still unclear why it is required. To address this question, we performed transcriptomic analysis on fluorescence-activated cell sorting (FACS) purified NF- $\kappa$ B<sup>+</sup> and NF- $\kappa$ B<sup>-</sup> ECs at the first peak of NF- $\kappa$ B activity (22–23 hpf) from *NF- $\kappa$ B:d2EGFP*<sup>+</sup>, *kdrl:mCherry*<sup>+</sup> embryos (Fig. 2A). As expected, NF- $\kappa$ B<sup>+</sup> and NF- $\kappa$ B<sup>-</sup> triplicates had the strongest correlation among all samples (Fig. Sup 3A). The Volcano plot illustrated the number of differentially expressed genes (DEGs) between NF- $\kappa$ B<sup>+</sup> and NF- $\kappa$ B<sup>-</sup> ECs (Fig. Sup 3B), with 2487 upregulated and 2248 downregulated genes with an adjusted *p* value (*p*-Adj)  $\leq 0.05$  (Fig. Sup 3C). Interestingly, when interrogating which NF- $\kappa$ B family members were enriched in the NF- $\kappa$ B<sup>+</sup> fractions, only p65 (*rela*) displayed significant upregulation (Fig. 2B). Gene Ontology (GO) enrichment analysis for upregulated biological processes in the *NF- $\kappa$ B*<sup>+</sup>, *kdrl*<sup>+</sup> fraction included signaling pathways critical during HSPC development such as non-canonical (*p*-Adj = 2.1e-07) and canonical (*p*-Adj = 9.8e-04) Wnt, EGFR1 (*p*-Adj = 3.9e-05), BMP (*p* Adj = 8.3e-4), TGF- $\beta$  (*p*-Adj = 0.010) and Delta-Notch (*p*-Adj = 0.155) (Fig. Sup 4A). Unexpectedly, GO terms downregulated in the *NF- $\kappa$ B*<sup>+</sup>, *kdrl*<sup>+</sup> fraction were primarily associated with cell division (Fig. Sup 4B). In addition, *NF- $\kappa$ B*<sup>+</sup> ECs showed a significant downregulation of key cell cycle genes such as mini-chromosome maintenance proteins (MCM), origin recognition complex (ORC), cell division control protein (CDC), etc. (Fig. 2C). These are essential regulators of the G<sub>1</sub>-S progression, DNA replication and/or G<sub>2</sub>-M checkpoints<sup>51–55</sup>. Cyclin-dependent kinase (CDK) inhibitors, including p21 (*CDKN1A*), p27 (*CDKN1B*), and p57 (*CDKN1C*), are key regulators of the cell cycle entry. While increased levels of CDK inhibitors promote quiescence, decreased levels are associated with exiting quiescence and entry into the cell cycle. Accordingly, *NF- $\kappa$ B*<sup>+</sup>, *kdrl*<sup>+</sup> ECs showed significant upregulation of the CDK inhibitors *cdkn1ba* and *cdkn1bb* (orthologous to human *cdkn1b*, or *p27*), and downregulation of *cdkn3* (Fig. 2D).

Decreased transcriptional activity occurs during cellular quiescence. Specifically, the binding of RNA polymerase I to rDNA is greatly reduced in G<sub>0</sub><sup>56</sup>, while increased RNA polymerase III activity is tightly linked to cell growth and proliferation<sup>57</sup>. Consistently, genes associated with “General transcription by RNA polymerase I”, and “RNA polymerase III transcription initiation” were significantly downregulated in *NF- $\kappa$ B*<sup>+</sup>, *kdrl*<sup>+</sup> ECs (Fig. 2E). Moreover, *NF- $\kappa$ B*<sup>+</sup> ECs transcriptomics displayed significantly downregulated GO terms related to mitochondrial function, including “Mitochondrial protein import”, “Mitochondrial translation elongation/termination”, and “the electron transport chain”, and reduced levels of reactive oxygen species (ROS), which are indicative of cellular quiescence (Fig. 2F). Finally, *NF- $\kappa$ B*<sup>+</sup>, *kdrl*<sup>+</sup> ECs showed significant downregulation of genes comprising the major subunits for cytochrome *c* oxidase (COX) and NADH:ubiquinone oxidoreductase, central to powering ATP production through oxidative phosphorylation (Fig. 2F), which is typically decreased in quiescent cells. Together, ECs with active NF- $\kappa$ B signaling prior to EHT suggested a potential role for p65 maintaining quiescence within the EC precursors of HSPCs.

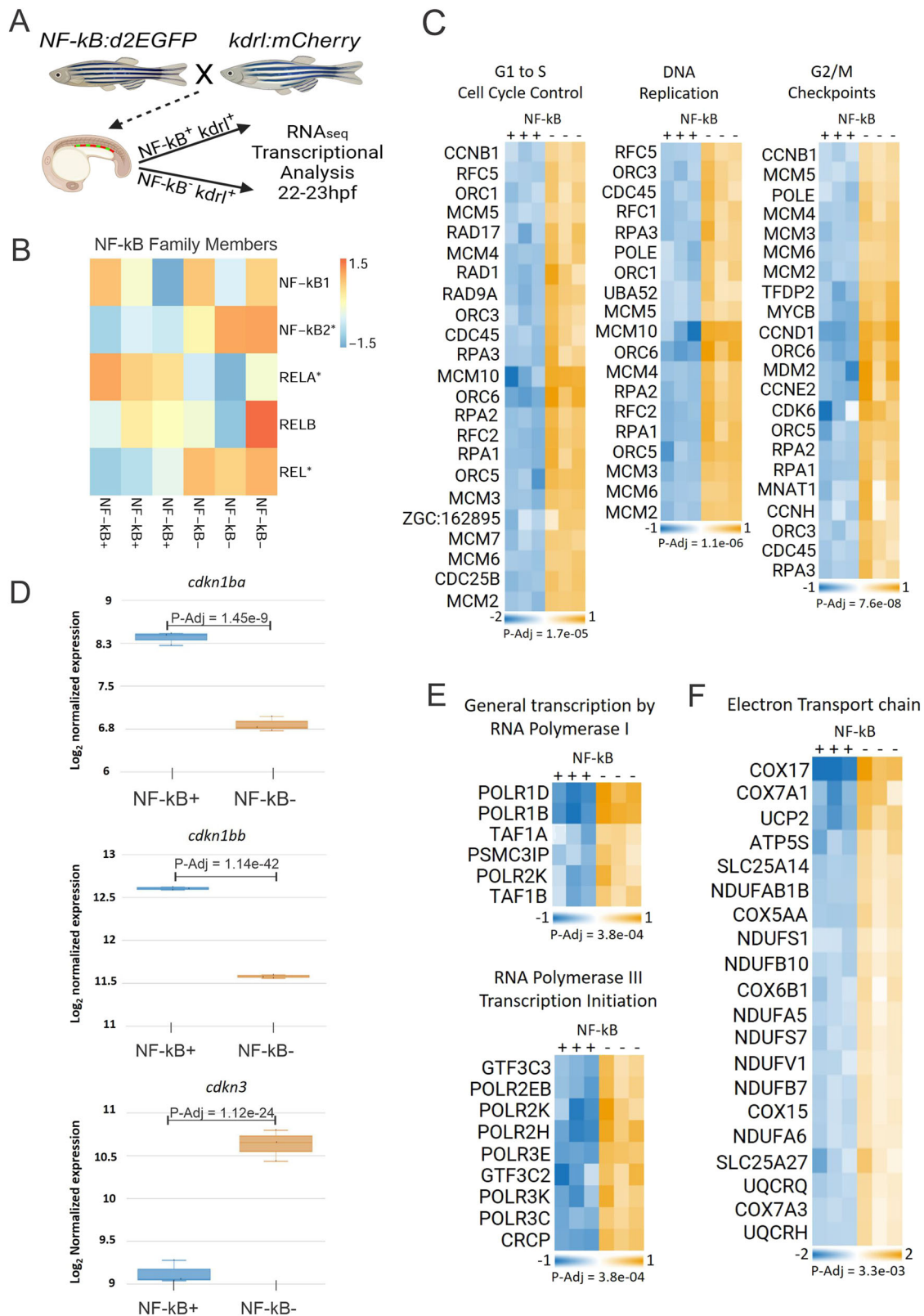
### The first wave of NF- $\kappa$ B activation is p65-dependent and critical for HE patterning

To address if NF- $\kappa$ B<sup>+</sup> ECs gave rise to HE, we generated an additional NF- $\kappa$ B reporter line (*NF- $\kappa$ B:D2mRFP*) that we crossed with one of the earliest hemogenic endothelium transgenic reporters currently available (*runx1P2:Citrine*)<sup>37</sup>. Confocal analysis of the DA at 24 hpf showed that all *runx1P2:Citrine*<sup>+</sup> HE cells within the DA were *NF- $\kappa$ B:d2mRFP*<sup>+</sup>, demonstrating the NF- $\kappa$ B<sup>+</sup> endothelial origin of the HE (Fig. 3A).

NF- $\kappa$ B is comprised of five family members (p50, p52, p65, RelB and c-Rel)<sup>58–60</sup>, however, the exact NF- $\kappa$ B member responsible for HSPC development and its temporal requirement is enigmatic. Since our transcriptomic analysis revealed p65 (also known as *rela*) as the only upregulated NF- $\kappa$ B family member gene in *NF- $\kappa$ B*<sup>+</sup> ECs at 22–23 hpf (Fig. 2B), we hypothesized that the first wave of NF- $\kappa$ B activation was p65-dependent. To test this hypothesis, we performed several p65 loss of function (lof) approaches, including the generation of a novel p65 zebrafish loss of function allele. First, we designed a specific guide RNA (gRNA) targeting Cas9 to a site near the beginning of the third exon of p65 (Sup Fig. 5A). Its mutagenesis efficiency was validated in Sup Fig. 5B–D. To address if p65 lof reduced NF- $\kappa$ B activity in the endothelium, we injected p65 gRNA with Cas9 into *Tg(NF- $\kappa$ B:d2EGFP; kdrl:mCherry)* embryos. Flow cytometric analysis at 22 hpf showed reduced NF- $\kappa$ B activity in the vasculature of the embryo (*kdrl*<sup>-</sup>), but no effect in non-vascular tissues (*kdrl*<sup>+</sup>) compared to p65 gRNA only controls (Fig. 3B, C). To determine if p65 lof resulted in decreased emergent HSPCs, we injected p65 gRNA with Cas9, or p65-MO, and their respective controls, into *Tg(kdrl:mCherry; Cd41:eGFP)* embryos. Live confocal analysis of *mCherry*<sup>+</sup>; *eGFP*<sup>+</sup> HSPCs at 52 hpf showed a significant reduction of HSPC numbers in p65 crispants and morphants compared to their respective controls (Fig. 3D and Fig. S6A). To address if p65 was required for the formation of the hemogenic endothelium (HE), we performed WISH at 26 hpf for the HE marker *runx1*<sup>61</sup> in p65 deficient embryos. As shown in Fig. S6B, the number of *runx1*<sup>+</sup> HE cells (HECs) was significantly diminished in p65 morphant embryos compared to Std-injected controls. Finally, to confirm the role of p65 in early HE specification, we generated a p65 stable loss of function allele in *rela* (p65) using GeneWeld CRISPR/Cas9 precision targeted integration of a Stop-PRISM cassette<sup>62–64</sup>. The transcription-terminating cassette was integrated into *rela* exon 3 (Fig. S5E, F; Methods). A precise integration allele was recovered to establish the transgenic line *Tg(rela-3XStop; he1a:mRFP)*<sup>65</sup> (referred to as *P65*<sup>STOP</sup>). We next performed WISH for HE markers<sup>18,61,65</sup> in inbred p65 heterozygous (*p65*<sup>STOP/+</sup> IC). Interestingly, both p65 heterozygous (*p65*<sup>STOP/+</sup>) and homozygous mutants (*p65*<sup>STOP/STOP</sup>) showed a significant decrease in HECs throughout their development compared to WT siblings (*p65*<sup>+/+</sup>) (Fig. 3E–G), suggesting that both p65 haploinsufficiency and complete lof failed to induce ECs towards a hemogenic fate.

To pinpoint the temporal window when NF- $\kappa$ B activity was required for HSPC development, we screened for chemical compounds known to diminish NF- $\kappa$ B activity. Caffeic acid phenethyl ester (CAPE), which has been shown to prevent p65 translocation to the nucleus in mammalian cell lines<sup>49</sup>, drastically reduced NF- $\kappa$ B activity within the trunk vasculature (*kdrl*<sup>-</sup>), but not in other tissues (*kdrl*<sup>+</sup>) (Fig. S7A), recapitulating the phenotype when using genetic p65 lof approaches. To confirm the inhibition of p65 by CAPE in zebrafish embryos, we performed cleavage under targets and release using nuclease qPCR (CUT&RUN-qPCR) for p65<sup>66</sup> at 22 hpf in 16–22 hpf CAPE-treated zebrafish embryos, or DMSO controls. As shown in Fig. S7B, C, the previously validated p65 binding sites (BS) 1, 2, 3, and 4 to *nfkb1aa* DNA regulatory sequences<sup>66</sup> showed statistically significant positive enrichment in DMSO-, but not in CAPE-treated embryos. As expected, no enrichment was found in either DMSO- or CAPE-treated embryos in the isotype immunoglobulin G control, or two previously validated negative binding control sites for p65 (negative BS1 and BS2)<sup>66</sup> (Fig. S7B, C). Finally, to demonstrate the specific inhibition of the NF-





κB program by CAPE, we chemically incubated AB WT embryos from 16–22 hpf and examined bona fide NF-κB responsive genes by qPCR<sup>67</sup> at 22 hpf. As expected, there was a significant downregulation of *il6*, *ikbaa*, and *il1b* expression, but not *p65* (*rela*) expression, even when using a lower CAPE dose (2 μM) to mimic the *p65* haploinsufficiency phenotype (Fig. S7D–G). To investigate a potential role for *p65* in cell survival, we performed Terminal deoxynucleotidyl transferase (TdT)

dUTP Nick-End Labeling (TUNEL) assay in *p65* mutants and CAPE-treated embryos, and found no significant differences when compared to their respective controls (Figs. S8A, B, S9A, B). Finally, endothelial (*kdrl*) and arterial (*efnb2a*) markers examined by WISH in CAPE-, and DMSO-treated embryos showed similar expression (Fig. S10A), suggesting that endothelial and arterial fate were not impaired after temporal disruption of *p65*. In summary, these results

**Fig. 2 | Transcriptomic analysis of NF- $\kappa$ B<sup>+</sup> ECs showed upregulated p65 and downregulated cell cycle-specific genes.** **A** Schematic of the experimental design followed in Fig. 2. *kdr1:mCherry* zebrafish were mated to *NF- $\kappa$ B:d2EGFP* to generate double transgenic *kdr1:mCherry<sup>+</sup>, NF- $\kappa$ B:d2EGFP<sup>+</sup>* embryos for subsequent bulk transcriptomic profiling of FACS purified ECs (**B–F**). **B** Heat map depicting transcript levels of NF- $\kappa$ B family members in NF- $\kappa$ B<sup>+</sup> versus *NF- $\kappa$ B<sup>-</sup> kdr1<sup>+</sup>* ECs. (\*) are statistically significant at <1% FDR. **C** Heat map depicting differentially expressed genes involved in G<sub>1</sub> to S cell cycle control (left), DNA replication (middle), and G<sub>2</sub>/M checkpoints in *NF- $\kappa$ B<sup>+</sup>* versus *NF- $\kappa$ B<sup>-</sup> kdr1<sup>+</sup>* ECs. **D** Box plots depicting differentially expressed cyclin-dependent kinase inhibitors in *NF- $\kappa$ B<sup>+</sup>* and *NF- $\kappa$ B<sup>-</sup> kdr1<sup>+</sup>* ECs. Data were generated from three biological replicates. *cdkn1ba* (for NF- $\kappa$ B<sup>+</sup>: Max = 8.4, Min = 8.2, Median = 8.4, Q1 = 8.2, Q3 = 0.0, for NF- $\kappa$ B<sup>-</sup>: Max = 7, Min = 6.7, Median = 6.8, Q1 = 6.7, Q3 = 7.0). *cdkn1bb* (for NF- $\kappa$ B<sup>+</sup>: Max = 12.6, Min = 12.6, Median = 12.6,

Q1 = 0.0, Q3 = 0.0, for NF- $\kappa$ B<sup>-</sup>: Max = 11.6, Min = 11.6, Median = 11.6, Q1 = 0.0, Q3 = 0.0). *cdkn3* (for NF- $\kappa$ B<sup>+</sup>: Max = 9.3, Min = 9.0, Median = 9.1, Q1 = 9.0, Q3 = 9.3, for NF- $\kappa$ B<sup>-</sup>: Max = 10.8, Min = 10.4, Median = 10.7, Q1 = 0.0, Q3 = 0.0). **E** Heat map showing differentially expressed genes involved in “general transcription by RNA polymerase I” (top) and “RNA polymerase III transcription initiation” (bottom) in *NF- $\kappa$ B<sup>+</sup>* versus *NF- $\kappa$ B<sup>-</sup> kdr1<sup>+</sup>* ECs. **F** Heat map depicting differentially expressed genes involved in the electron transport chain in *NF- $\kappa$ B<sup>+</sup>* versus *NF- $\kappa$ B<sup>-</sup> kdr1<sup>+</sup>* ECs. For the heatmaps in (C, E, F), all genes depicted are statistically significant at FDR-adjusted *p* values at or below the values listed. DESeq2 was used to calculate fold changes and *p* values and perform optional covariate correction (C–F). Figure 2A created with BioRender.com released under a Creative Commons Attribution-NonCommercial-NoDeriv 4.0 International license.

demonstrate that in ECs, CAPE abolishes the transcriptional activity of the zebrafish ortholog p65, and therefore it can be used to temporally block p65 activity within the embryonic developing vascular cord. Moreover, we showed that the early NF- $\kappa$ B activation wave, which occurs prior EHT (16–24hpf), is p65-dependent and critical to induce ECs towards a hemogenic fate.

### p65 is required for HSPC development, but not for the primitive or EMP hematopoietic developmental programs

Vertebrate embryonic hematopoiesis occurs through two waves. While primitive hematopoiesis produces primitive erythroid and myeloid cells, definitive hematopoiesis generates erythromyeloid progenitors (EMPs) and HSPCs<sup>35,68–70</sup>. To identify if both hematopoietic programs were driven by NF- $\kappa$ B signaling, we lived imaged *kdr1:mCherry<sup>+</sup>, NF- $\kappa$ B:d2EGFP<sup>+</sup>* embryos at 16hpf and 19hpf by confocal microscopy. Zebrafish is an advantageous system, since primitive myelopoiesis is anatomically separated from definitive hematopoiesis<sup>71</sup>. Rostral *kdr1<sup>+</sup>* ECs were mostly *NF- $\kappa$ B<sup>-</sup>*, while *kdr1<sup>+</sup>*, NF- $\kappa$ B<sup>+</sup> ECs were identified within the medium-posterior part of the embryo (Fig. S10B), where definitive HECs develop. Next, we treated embryos from 16hpf with 5  $\mu$ M CAPE to inhibit the first NF- $\kappa$ B activity wave and performed WISH for the erythroid (*gata1*), macrophage (*mfap4*), and pan-leukocyte (*l-plastin*) markers at 22hpf to assess primitive hematopoiesis, as well as the definitive HE markers *gata2b*, *runx1*, and *cmyb* after ~22hpf. As shown in Fig. S11A–G, primitive erythroid, myeloid, and EMP cell numbers were unaffected. In contrast, CAPE-treated embryos displayed a profound decrease in all HE markers (Fig. 4A, B). To identify if p65 was required throughout the entire first temporal window of NF- $\kappa$ B activation (16–24hpf), we inhibited p65 in three sub-temporal blocks of 3 h by incubating *Tg(kdr1:mCherry; cd41:eGFP)* embryos with 5  $\mu$ M of CAPE. Flow cytometric analysis for *cd41<sup>+</sup>* (Fig. 4C), and WISH for *cmyb* (Fig. 4D, E) showed a partial loss of developing HSPCs after NF- $\kappa$ B inhibition, with the most profound reduction occurring when p65 was blocked from 20 to 23hpf, correlating with the NF- $\kappa$ B activity levels described above. This suggests that NF- $\kappa$ B functions throughout the entire developmental window of HE induction. Altogether, these observations demonstrate that the first wave of NF- $\kappa$ B activity is dispensable for EMP and primitive hematopoiesis, but necessary to pattern the definitive HE for HSPC specification.

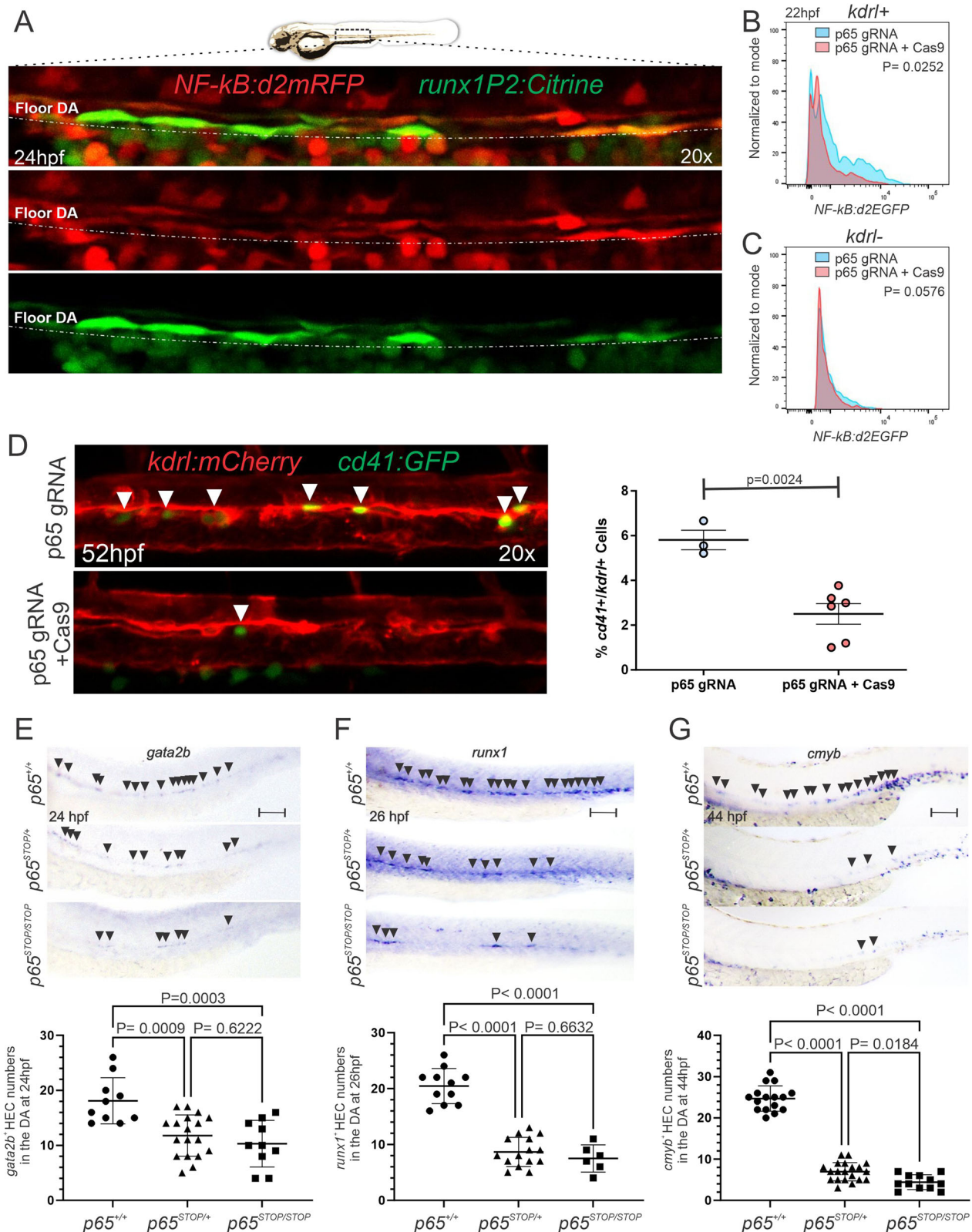
### P65-induced quiescence in ECs is a prerequisite to become hemogenic

Our results demonstrated the critical role of p65 during HSPC specification. However, it is unclear the cellular function that p65, and pro-inflammatory signaling in general, exerts within ECs to drive their competency toward HSPC fate. NF- $\kappa$ B regulates different and contrasting biological functions, including survival, apoptosis, inflammation, regeneration, and senescence<sup>72,73</sup>. However, our transcriptomic data showed significant downregulation of key genes affiliated with a proliferative state (Fig. 2 and Fig. S4). Therefore, we hypothesized that p65 might induce a reversible arrest of the cell cycle that would

prevent ECs from cell cycle entry. To test this, we performed cell cycle analysis by flow cytometry in NF- $\kappa$ B<sup>+</sup> and NF- $\kappa$ B<sup>-</sup> ECs from embryonic trunks at 22hpf. As shown in Fig. 5A, B, the majority of NF- $\kappa$ B<sup>+</sup> ECs were in G<sub>0</sub>-G<sub>1</sub> (~82%), with a small percentage of cells in S (~15%) or G<sub>2</sub>-M (~1%), while NF- $\kappa$ B<sup>-</sup> ECs were significantly more proliferative (G<sub>0</sub>-G<sub>1</sub>, ~53%; S, ~26%; G<sub>2</sub>-M, ~17%). The low mitotic rate within the NF- $\kappa$ B<sup>+</sup> ECs was assessed by whole-mount immunohistochemistry (WIBC) for the mitotic marker phospho-histone H3 (Ser10) (pH3), in 22hpf *kdr1:mCherry<sup>+</sup>, NF- $\kappa$ B:d2EGFP<sup>+</sup>* embryos. Confocal analysis showed that mitotic *kdr1<sup>+</sup>* ECs had NF- $\kappa$ B inactive (Fig. 5C and Fig. S12). To address if NF- $\kappa$ B was the cause of EC quiescence, we performed intracellular flow for pH3 in *kdr1:mCherry<sup>+</sup>, NF- $\kappa$ B:d2EGFP<sup>+</sup>* embryonic trunks at 22hpf. While ~8% of all *kdr1<sup>+</sup>* ECs (*NF- $\kappa$ B<sup>-</sup>*) treated with DMSO were in mitotic phase (Fig. 5D, E), ~12% of *kdr1<sup>+</sup>, NF- $\kappa$ B<sup>-</sup>* were pH3<sup>+</sup> (Fig. 5D, E'), whereas ~2% of *kdr1<sup>+</sup>, NF- $\kappa$ B<sup>+</sup>* ECs were proliferating (Fig. 5D, E''). In addition, these proliferative NF- $\kappa$ B<sup>+</sup> ECs were observed only in the NF- $\kappa$ B<sup>low</sup> fraction (Fig. 5E''). Since NF- $\kappa$ B haploinsufficiency recapitulated the HSPC phenotype observed in null mutants (Fig. 3E–G and S7E–G), we next utilized a lower dosage (2  $\mu$ M) of the p65 inhibitor CAPE to reduce NF- $\kappa$ B activity without completely abolishing it, therefore allowing for detection of partial NF- $\kappa$ B activation by the reporter. With the treatment of 2  $\mu$ M CAPE, *kdr1<sup>+</sup>, NF- $\kappa$ B<sup>-</sup>, pH3<sup>+</sup>* ECs significantly increased from ~2 to ~9% (Fig. 5D, F''). This increase of proliferative NF- $\kappa$ B<sup>+</sup> ECs was also observed in the NF- $\kappa$ B<sup>low</sup> fraction (Fig. 5F''). These results, together with the transcriptomic data, demonstrate that high levels of NF- $\kappa$ B activity renders ECs quiescent, a prerequisite for their subsequent transdifferentiation into HSPCs<sup>74</sup>.

### The function of p65 in HE patterning is conserved during the development of definitive human hematopoietic progenitors

To address whether p65 was also required during human definitive HE patterning, we first queried if NF- $\kappa$ B was activated at single-cell resolution using a published transcriptomic dataset from in vitro iPSC-derived human definitive uncommitted hematopoietic progenitors and primed differentiated hematopoietic lineages<sup>75</sup>. As shown in Fig. Sup. 13, multiple known NF- $\kappa$ B target genes, including *NFKBIA*, *BCL3*, *HIF1A*, *SPI1*, *RELB*, and *CTSB*<sup>76</sup>, were significantly upregulated throughout the hematopoietic developmental trajectory, suggesting a conserved and essential role for NF- $\kappa$ B signaling during human hematopoietic development. To test this, we inhibited or over-activated p65 during the HE-like patterning phase by 5  $\mu$ M CAPE, or the Nod1 agonist C12-iE-DAP, which we previously demonstrated to activate NF- $\kappa$ B<sup>40</sup> (herein called C12), respectively, between days 4–5 of differentiation. These experiments were performed using the protocol established by Sturgeon and colleagues to derive definitive hematopoiesis by Wnt activation and activin-nodal inhibition at day 2 from iPSCs<sup>77</sup> (Fig. S14A). While p65 inhibition resulted in a profound reduction in the CD34<sup>+</sup>/CD184<sup>-</sup>/CD73<sup>-</sup> fraction at day 9, which is known to contain the HE-like cells<sup>78</sup>, cells treated with C12 exhibited a significant increase in the CD34<sup>+</sup>/CD184<sup>-</sup>/CD73<sup>-</sup> fraction when compared to the DMSO control (Fig. S14B). Further analysis of the CD34<sup>+</sup>/CD43<sup>-</sup>



endothelial profiles at day 9 revealed that CAPE-treated cells exhibited a significantly higher percentage of CD184<sup>+</sup>/CD73<sup>+</sup> arterial endothelial progenitors when compared to C12 and the DMSO control (Fig. S14C, D). Next, intracellular flow for RUNX1 (commonly used marker of HE<sup>79</sup> within the CD34<sup>+</sup>/CD43<sup>-</sup> fraction) at day 9 showed a 6-fold reduction in the CAPE-treated condition (Fig. S14E). Next, to functionally demonstrate the loss of HE-like potential after p65 inhibition, at day 9, we

sorted and aggregated an equivalent number of CD34<sup>+</sup>/CD43<sup>-</sup> cells/well previously treated with CAPE, or control DMSO, from day 4–5 and quantified the number of budding hematopoietic progenitor cells (HPCs) at day 9 + 7. As shown in Fig. S14F, G, p65 inhibition decreased over 1000-fold the ability of the CD34<sup>+</sup>/CD43<sup>-</sup> population to form HPCs. Next, we aimed to investigate the cell cycle during iPSC definitive hematopoietic differentiation in cells treated with CAPE or C12



**Fig. 3 | p65 drives hemogenic endothelium patterning during HSPC development.** **A** Representative 20x maximum projection confocal images from 24 hpf *Nfkb:td2mRFP*; *runx1P2:Citrine*<sup>+</sup> embryos showing that all *runx1*<sup>+</sup> cells are NF-kB<sup>+</sup> in the floor of the DA. The experiment was repeated three times independently with similar results. **B, C** Representative histograms depicting flow cytometric analysis of 5–10 pooled 22hpf trunks isolated from *Nf-kb:d2EGFP*; *kdr1:mCherry*<sup>+</sup> embryos injected with p65 gRNA only (blue) or p65 gRNA + Cas9 (red). *Nf-kb*<sup>+</sup>/*kdr1*<sup>+</sup> EC population (**B**), *Nf-kb*<sup>+</sup>/*kdr1*<sup>-</sup> non-EC population (**C**) (normalized to mode). **D** Representative 20x maximum projection confocal images from F<sub>0</sub> 52hpf *cd41:eGFP*; *kdr1:mCherry*<sup>+</sup> injected with p65 gRNA only (control), or p65 gRNA + Cas9

(left panel), and quantifications by flow cytometric analysis of 5–10 pooled embryos (right). p65 gRNA only ( $n = 3$ ) and p65 gRNA + Cas9 ( $n = 6$ ). **E, G** Representative bright-field images (top panels) of *p65*<sup>+/+</sup>, *p65*<sup>STOP/+</sup>, and *p65*<sup>STOP/STOP</sup> embryos at the indicated stages subjected to WISH for the HE markers *gata2b*, *runx1*, and *cmyb*, followed by genotyping, and their quantifications (bottom panels). Each dot represents an individual embryo. Black arrowheads denote HECs on the floor of DA. Scale bar = 100  $\mu$ m. Black horizontal lines indicate mean  $\pm$  SD (Black). Data were analyzed by unpaired two-tailed *T*-test (**B–D**) or ordinary one-way ANOVA with Turkey's multiple comparisons test (**E–G**). Source data are provided as a Source Data file.

(between days 4–5), at day 6 (immediately following treatment) and day 9 (4 days post treatment). At day 6, no significant differences within the CD34<sup>+</sup>/CD43<sup>-</sup> populations were observed across all conditions (Fig. S15A). To assess the cell cycle, EB's were dissociated at T6 and T9 and stained for CD34, Ki67, and DNA FxCycle Violet as described in the methods section. At day 6, very few cells were CD34<sup>+</sup>, making it difficult to segregate out the G<sub>0</sub> and G<sub>1</sub> phases in this fraction. For this reason, G<sub>0</sub> and G<sub>1</sub> were combined for analysis of the CD34<sup>+</sup>/CD43<sup>-</sup> population. As shown in Fig. S15B–B', D, CAPE significantly decreased the percentage of cells in G<sub>0</sub>-G<sub>1</sub> (-58%), while C12 increased it (-77%), as compared to DMSO (-71%). In addition, a twofold increase was observed in the percentage of cells in G<sub>2</sub>/M phase in CAPE (-14%) treated cells when compared to the C12 (-7%) condition (Sup Fig. S15B–B', D). When all cells at day 6 were analyzed for cell cycle, a significant difference was only observed in the G<sub>1</sub> phase between CAPE (-16%) and C12 (-26%) treated cells (Sup Fig. S15C–C", E). By day 9 (4 days post treatment), no significant differences were observed across all conditions in regard to the percentage of the CD34<sup>+</sup>/CD43<sup>-</sup> populations (Fig. S16A). In addition, no differences were observed in the percentages of cells in each phase of the cell cycle across all treatments in both the CD34<sup>+</sup>/CD43<sup>-</sup> and *All Cell* fractions (Fig. S16B–E). Together, these results show that similarly to zebrafish, p65 activation is critical to regulate cell cycle and induce human endothelial-like cells to become hemogenic for the formation of definitive human HPCs.

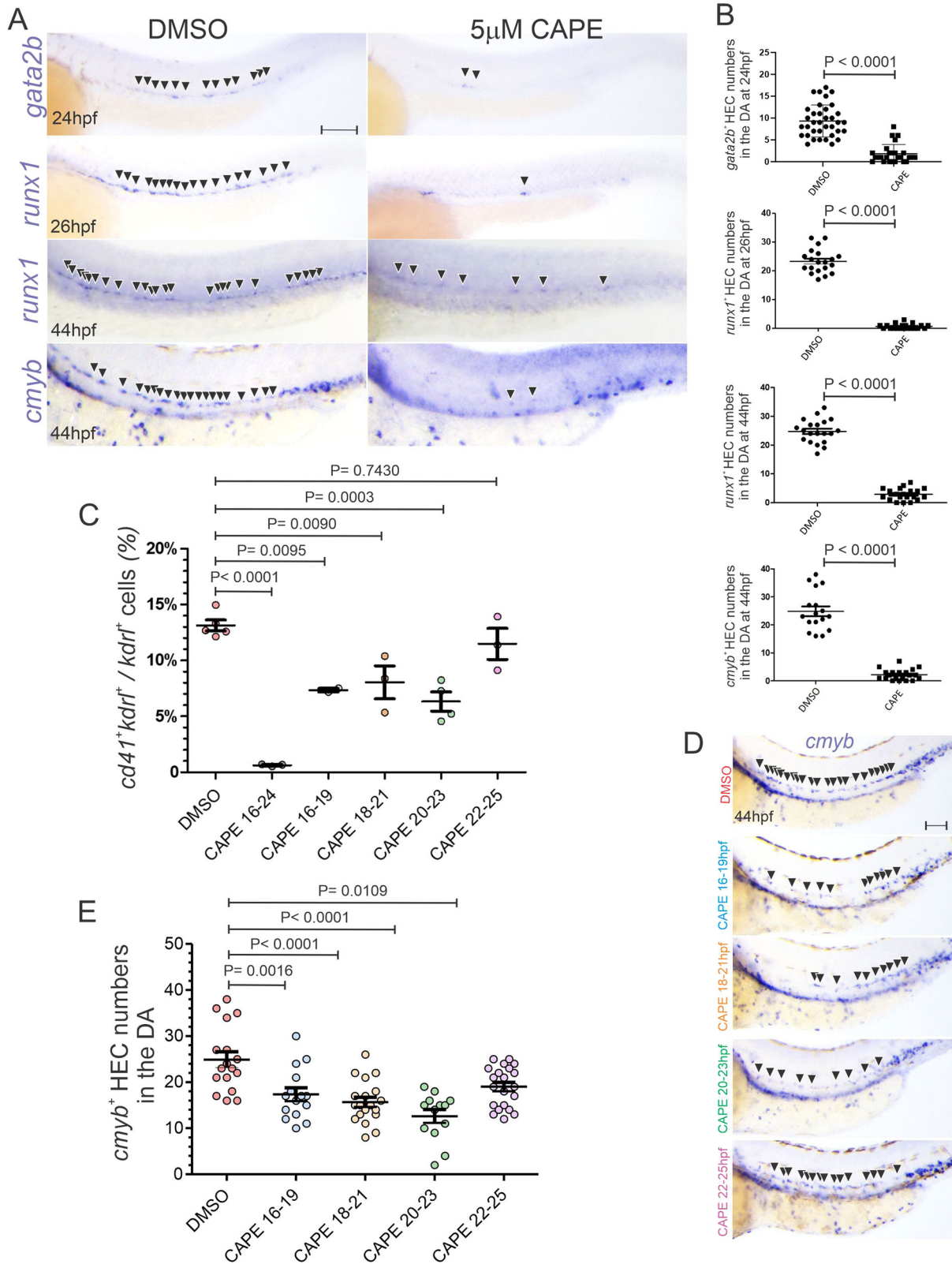
### Lineage tracing at the single-cell resolution revealed NF-kB reactivation within aortic ECs

We demonstrated that NF-kB activated in two waves within the ECs of the aorta region. However, whether the first and second NF-kB activity waves occurred within the same EC was unclear. To address this question, we generated an NF-kB reporter zebrafish driving the photoconvertible protein Kaede under the NF-kB responsive elements, *Tg(Nfkb:Kaede)*<sup>js04</sup>. A nuclear eGFP vascular endothelial reporter transgenic *-Tg(fli:nEGFP)*<sup>80</sup> was crossed to *Tg(Nfkb:Kaede)* to track the NF-kB activity within individual ECs. We reasoned that if *Nfkb:Kaede* was photoconverted from green to red by UV exposure after the first NF-kB wave was completed (25 hpf), then two putative scenarios could occur (Fig. 6A). First, if the first and second NF-kB activity waves occurred in different ECs, either Kaede (green) or photoconverted Kaede (red) cytoplasmic ECs would be identified. In contrast, if both NF-kB activity waves occurred within the same EC, newly produced cytoplasmic Kaede (green) would colocalize with 25 hpf photoconverted Kaede (red). Fig. S17 shows a representative *Nfkb:Kaede*; *fli:nEGFP*<sup>+</sup> before (25 hpf) and after (25.25 hpf) Kaede photoconversion. As shown in Fig. 6B, the majority of photoconverted Kaede (red cytoplasm) colocalized with newly generated non-photoconverted Kaede (green cytoplasm) within the floor of the DA (ventral green nuclei) by confocal microscopy at 34hpf. A few ECs within the floor of the DA with only Kaede red, but not Kaede green, cytoplasm were observed, possibly due to an asynchronous delamination of HSPCs. In addition, we observed that NF-kB<sup>+</sup> ECs during the second wave of NF-kB activity were in a non-proliferative state (Fig. S18). Together, these results demonstrate that the first and second NF-kB activity waves

occur within the same ECs, and that NF-kB activation negatively regulates the cell cycle.

### Time-specific manipulation of NF-kB during EHT leads to HSPC expansion

To investigate if NF-kB played a role in HSPC development during the NF-kB reactivation phase (-32hpf) (Fig. 1C), we allowed the first NF-kB wave to naturally occur (16–24hpf) to permit for HE induction, and then incubated AB and *Tg(cd41:GFP*; *kdr1:mCherry*) embryos with 5  $\mu$ M CAPE, or DMSO control, from 28hpf. Unexpectedly, we observed a robust increase of HECs (*cmyb*<sup>+</sup> and *gata2b*<sup>+</sup>) in the DA (Fig. 7A), and *cd41:GFP*<sup>+</sup>; *kdr1:mCherry*<sup>+</sup> HSPCs (Fig. 7B), in CAPE-treated embryos. In contrast, there was a decrease in the colonization of the CHT of *cmyb*<sup>+</sup>, *gata2b*<sup>+</sup>, (Fig. 7A, red dashed boxes), and *cd41:GFP*<sup>+</sup> developing HSPCs (Fig. 7C). Flow cytometric analysis showed a 2-fold increase of total *cd41*<sup>+</sup> cells per 4 pooled embryos after CAPE treatment from 28hpf (Fig. 7D). Together, these data suggested that NF-kB inhibition during the NF-kB reactivation phase (28–36hpf) not only impaired HSPC migration from the DA to the CHT, but also expanded the number of developing HSPCs within the DA. We then hypothesized that this expansion was due to: (1) the elongation of the “NF-kB OFF phase”, resulting in a proliferative expansion within the DA; and (2), failure of HSPCs to undergo EndoMT. To test this, 72hpf *cd41:GFP*<sup>+</sup>; *kdr1:mCherry*<sup>+</sup> embryos were live imaged after treatment with DMSO or CAPE from 28hpf. At 72hpf, DMSO control embryos lacked emergent HSPCs at 72hpf in the DA (Fig. S19A, white rectangle) since they already migrated to the caudal hematopoietic tissue (CHT) (analog to the mammalian fetal liver). However, embryos treated with CAPE displayed a continued expansion of *cd41*<sup>+</sup> cells throughout the DA and minimal colonization of the CHT and thymus (Fig. S19A, B). Large *cd41*<sup>+</sup> aortic clusters forming within the ventral floor of the DA were identified only after CAPE treatment (Fig. 8A and S20). These clusters are not present naturally in zebrafish, suggesting that due to a brief “NF-kB resolution phase”, HECs minimally expand in the aortic niche. WISH from 72hpf AB embryos treated with DMSO or CAPE from 28–72hpf revealed that *runx1*<sup>+</sup> and *cmyb*<sup>+</sup> HECs persisted within the DA in CAPE-treated embryos, whereas these mainly localized in the CHT in control embryos (Fig. 8B, red arrows). To test if the *cd41*<sup>+</sup> clusters in the DA after NF-kB inhibition from 28hpf were formed, at least in part, due to a proliferative expansion, WIHC was performed for pH3 on *cd41:GFP*<sup>+</sup>; *kdr1:mCherry*<sup>+</sup> embryos treated with DMSO or CAPE. *cd41*<sup>+</sup>; pH3<sup>+</sup> mitotic HSPCs within the DA were found in CAPE-treated embryos at 72hpf (Fig. 8C), and in the CHT region of DMSO control and CAPE-treated embryos at 72hpf (Fig. 8D). In addition, *cd41*<sup>+</sup>; pH3<sup>+</sup> cells were identified in large clusters in the DA of CAPE-treated embryos (Fig. 8E). Flow cytometric analysis on *cd41:GFP*<sup>+</sup>; *kdr1:mCherry*<sup>+</sup> embryos treated with CAPE from 28hpf displayed a significant increase in the total number of *cd41*<sup>+</sup> HSPCs at 72hpf (Fig. 8F). When CAPE was removed at 72hpf, elevated *cd41*<sup>low</sup> numbers were still detected at 120hpf (Fig. 8G). Moreover, key biomarkers of epithelial-mesenchymal transition were significantly upregulated in the NF-kB<sup>+</sup> versus NF-kB<sup>-</sup> ECs at 22 hpf in our transcriptomic data (Fig. 2A and S21). Together, these results demonstrate that NF-kB reactivation is required for HSPC delamination from the DA and cell cycle control.



**Discussion**

Most gene functions have been discovered through phenotypic observations under loss of function experiments that lack temporal control. However, cell signaling is convergent, and the number of transcriptional effectors limited, having to be re-used and co-opted temporally and spatially within the organism. Despite this, the dynamic nature of signaling pathways have been often overlooked due to the

difficulty on their assessment, resulting in important bottlenecks in biology. Through the generation of novel NF-κB reporter zebrafish embryos, *Tg(NF-κB:d2EGFP)<sup>is502</sup>* and *Tg(NF-κB:d2mRFP)<sup>is503</sup>*, containing destabilizing elements fused to fluorophores<sup>48,81</sup> driven by human NF-κB recognizing elements<sup>45</sup>, we visualized in real time that pro-inflammatory signaling is oscillatory, and that these oscillatory dynamics power an embryonic developmental clock that controls the

**Fig. 4 | The first wave of p65 activity is essential for the specification of the HE.**

**A** WISH for the HEC markers *gata2b*, *runx1*, and *cmyb* at the indicated stages in AB embryos treated with DMSO (left panels) or 5  $\mu$ M CAPE (right panels) from 16–24hpf. Black arrowheads denote HECs in floor of DA. Scale bar = 100  $\mu$ M. **B** Quantification of *gata2b*<sup>+</sup>, *runx1*<sup>+</sup>, and *cmyb*<sup>+</sup> cells from (A). Each dot represents the number of HECs per embryo. **C** Percentage of *cd41*<sup>+</sup>, *kdrl*<sup>+</sup> cells within the total *kdrl*<sup>+</sup> EC fraction at 52hpf assessed by flow cytometry from *cd41:eGFP*; *kdrl:mCherry* embryonic trunks treated with DMSO or 5  $\mu$ M CAPE from 16–19hpf, 18–21, 20–23hpf, 22–25hpf, and 16–24hpf. Each dot represents 10–15 surgically isolated embryonic trunks from *cd41:eGFP*; *kdrl:mCherry* embryos. DMSO ( $n = 5$ ), 5  $\mu$ M

CAPE from 16–19hpf ( $n = 2$ ), 18–21hpf ( $n = 3$ ), 20–23hpf ( $n = 4$ ), 22–25hpf ( $n = 3$ ), and 16–24hpf ( $n = 3$ ). **D** Representative bright-field images of WISH for the HEC marker *cmyb* in 44hpf AB embryos treated with DMSO (red) or 5  $\mu$ M CAPE-treated embryos from 16–19hpf (blue), 18–21 (orange), 20–23hpf (green), and 22–25hpf (violet). Black arrowheads denote HECs in floor of DA. Scale bar = 100  $\mu$ M. **E** Quantification of *cmyb*<sup>+</sup> cells from (D). Each dot represents the number of *cmyb*<sup>+</sup> HECs per embryo. Black horizontal lines indicate mean  $\pm$  SD. Data were analyzed by unpaired two-tailed *T*-test (B) or ordinary one-way ANOVA with Turkey's multiple comparisons test (C, E). Source data are provided as a Source Data file.

progression of stem cell formation (Fig. 9). These signaling dynamics were missed using traditional reporter lines driving eGFP by the same NF- $\kappa$ B recognizing elements<sup>45</sup> due to the high stability of the eGFP mRNA and protein<sup>47</sup>. The discovery in this work of two distinct intrinsic NF- $\kappa$ B oscillatory waves during hematopoietic stem cell development, together with the use of a p65-specific inhibitor (CAPE), allowed for the first time the precise temporal inhibition of NF- $\kappa$ B signaling dynamics in vivo, which resulted in astonishing contrasting phenotypic outcomes. This highlights the importance of identifying carefully the signaling dynamics that drive cell fate, which will require the use of fluorophores fused to destabilizing elements instead of classical non-engineered ones<sup>82</sup>, whose perdurance is beyond 26 h<sup>47</sup>. Identifying the exact signaling dynamics in each particular cellular context could help resolve some of the conflicting work published regarding the role of signaling pathways during stem cell specification.

We show that the zebrafish embryo offers an advantageous platform to discover signaling dynamics in vivo difficult to achieve in other systems. Its external development, aquatic nature, and transparency, allows for the direct visualization of destabilized fluorophores, and for incubations with small chemicals that allow high penetrance and circumvent the challenging conditions of working *intra uteris*. Moreover, the zebrafish's rapid embryonic development (occurring within only 2 days) shorten considerably the experimental time, making this animal the perfect model to empower the discovery of signaling dynamics across time. In agreement with our work, a few studies have also suggested that other signaling pathways acted multiple times across development in the same biological process, suggesting that signaling dynamics is a universal trait that characterizes cell signaling to drive cell fate. For example, Kim et al. demonstrated that at least two waves of Notch activity were required during HSPC emergence in the zebrafish embryo<sup>83</sup>. Expanding these transgenic reporter tools to other pathways will be necessary to fully understand cell signaling dynamics for their recapitulation in vitro to derive the desired cell type from iPSC or organoids. Fortunately, some of these zebrafish transgenic reporters are already available<sup>48,84,85</sup>.

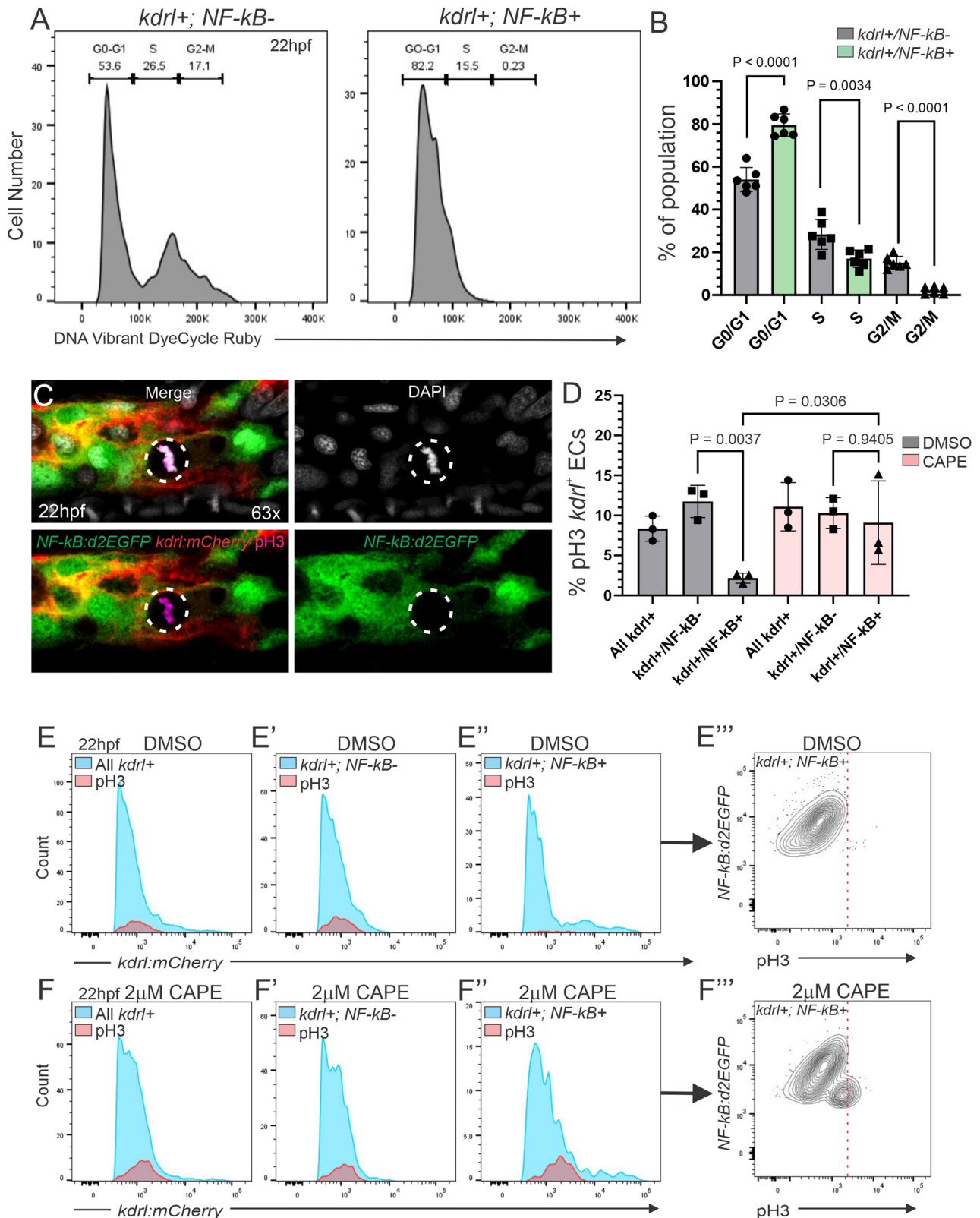
The identification in a temporal-specific manner of the combination of factors and inhibitors required to drive specification of HSPC fate has challenged the hematopoietic field for decades, hindering our efforts to efficiently derive human HSPCs. Here, we identified in vivo the temporal dynamics of NF- $\kappa$ B, a central regulator of HSPC fate<sup>25,40,43</sup>. We have revealed how pro-inflammatory pathways are leveraged in the aseptic embryo at two distinct stages during HSPC development to both priming ECs to become hemogenic, and later facilitate their detachment from the aortic floor. We observed by live imaging a significant increase in the percentage of *NF- $\kappa$ B*<sup>+</sup>; *kdrl*<sup>+</sup> ECs in the embryonic trunk region beginning at 16hpf<sup>40</sup> and peaking around 22hpf, just prior to the onset of expression of HE markers. This was followed by an abrupt deactivation at 26hpf, resembling the resolution of the inflammation phase documented in the context of injury and infection. Taking into account the -2 h of perdurance associated with the destabilized eGFP (d2EGFP)<sup>81</sup>, this suggests that the deactivation of NF- $\kappa$ B occurs around 24hpf, coinciding with the onset of the first embryonic heartbeats and the initiation of blood flow. Further studies will be needed to formally address if blood flow triggers NF- $\kappa$ B

inactivation. Interestingly, this deactivation was soon followed by a second wave of NF- $\kappa$ B reactivation at 32hpf, which was spatially restricted to endothelial cells located within the ventral floor of the DA, the site of definitive hematopoiesis. This proliferative expansion in the aorta was also observed in the zebrafish embryo from 26–32hpf<sup>9</sup> and in the mouse embryo<sup>86</sup>, supporting our findings. However, we were able to prolong artificially this proliferative phase until 72hpf by inhibiting p65 from 28hpf, which resulted in a -2-fold increase in *cd41*<sup>+</sup> cells that clustered within the floor of the DA and failed to delaminate and seed the CHT or thymus. The overactivation of the first NF- $\kappa$ B wave, and prolongation of the NF- $\kappa$ B OFF phase in in vitro protocols of human hematopoietic differentiation could increase the HSPC yield, facilitating human disease modeling and, perhaps, the production of human transfusion products. For future studies, however, it would be critical to identify if artificially amplified HSPCs maintain their functionality.

Despite the clear contribution of NF- $\kappa$ B to HSPC fate in vivo, the exact cellular outcome provided by this signaling pathway was unknown prior to the studies presented here. Our transcriptomics data from FACS isolated *NF- $\kappa$ B*<sup>+</sup> and *NF- $\kappa$ B* *kdrl*<sup>+</sup> ECs at the first peak of NF- $\kappa$ B activity (22hpf) showed a remarkable upregulation of hallmark molecular pathways required for HSPC specification such as Wnt, BMP, TGF- $\beta$ , and small Rho GTPases. Whether the activation of these pathways rely on NF- $\kappa$ B activity, act upstream NF- $\kappa$ B, or are independent of NF- $\kappa$ B signaling would need further assessment. The top downregulated GO terms associated with the *NF- $\kappa$ B*<sup>+</sup> EC signature were “cell cycle progression”, “proliferation”, “mitochondrial function”, and “RNA transcription”, all major features of a quiescent cell state. This was unexpected, since in other contexts, mainly pathological or during inflammation, p65 is known to drive proliferation<sup>87,88</sup>, cell survival, or apoptosis<sup>89</sup>. However, our studies in a developmental scenario highlight the importance of the environment, which results in different cellular outputs. Together with our transcriptomic analysis, intracellular flow and confocal imaging after mild NF- $\kappa$ B inhibition to allow for *NF- $\kappa$ B*<sup>+</sup> EC visualization, demonstrated that NF- $\kappa$ B (and particularly p65), is the driver of cell quiescence rather than a causative effect. We also show the haploinsufficiency effect of NF- $\kappa$ B signaling by genetic and chemical manipulations of p65, indicating that only high levels of NF- $\kappa$ B activity drive HSPC development by restraining the cell cycle. Together, these data suggest that prior to EHT, NF- $\kappa$ B signaling keeps ECs in a dormant stage, and this could be, at least partially, what classically has been referred to as “endothelial priming” towards hemogenic. These findings unveil a new functional output never before linked to NF- $\kappa$ B signaling, resolving how pro-inflammatory signaling contributes to natural development. Our findings agree with a recent report showing decreased long-term HSCs within I $\kappa$ B $\alpha$  deficient mice embryos, and their impaired maturation and low proliferation<sup>90</sup>. The authors found that loss of I $\kappa$ B $\alpha$  induced a dormancy-related gene expression signature in developing HSCs. Thus, it is plausible that I $\kappa$ B $\alpha$ , a well-known inhibitor of p65, participates in the p65 shutdown after ECs are specified, and without which, p65 fails to turn off, and HE fails to expand.

To the best of our knowledge, this is the first report demonstrating that NF- $\kappa$ B can trigger cell quiescence. Exactly how the activation of pro-inflammatory pathways yields different outcomes during





early development as opposed to classical inflammation or cancer, remains unclear.

The NF- $\kappa$ B transcription factor family is comprised of five structurally related subunits (NF- $\kappa$ B1 p50, NF- $\kappa$ B2 p52, RELA -also called p65-, RELB, and c-REL<sup>91</sup> that activate canonical (p65-dependent), or non-canonical NF- $\kappa$ B signaling<sup>89,92</sup>. All these NF- $\kappa$ B members contain a highly conserved Rel homology domain that facilitates both

dimerization and DNA binding to a similar consensus sequence<sup>93</sup>, and that presumably could activate our custom NF- $\kappa$ B reporter embryos. Nevertheless, our transcriptomic data identified p65 as the only significantly upregulated NF- $\kappa$ B family member in NF- $\kappa$ B<sup>+</sup> ECs prior to blood flow. Utilizing genetic and chemical loss of function approaches for p65 revealed that the first wave of NF- $\kappa$ B activity was p65-dependent. This is in agreement with our recent work demonstrating

**Fig. 5 | P65 drives EC quiescence prior to endothelial to hematopoietic transition.** **A** Representative histograms of live *kdrl:mCherry*<sup>+</sup>; *NF-kB:d2EGFP*<sup>+</sup> (left) and *kdrl:mCherry*<sup>+</sup>; *NF-kB:d2EGFP*<sup>-</sup> cells (right) from 15–20 pooled 22hpf isolated trunks stained with DNA Vibrant DyeCycle Ruby. Brackets denote resting/Gap 1 phase (G<sub>0</sub>-G<sub>1</sub>), Synthesis phase (S), and Gap 2/Mitotic phase (G<sub>2</sub>-M). **B** Quantification from (A). Each dot represents 15–20 pooled embryonic trunks, *n* = 6. Black horizontal lines indicate mean ± SD. **C** Representative confocal maximum projection image of the DA of a 22hpf *NF-kB:d2EGFP*<sup>+</sup>; *kdrl:mCherry*<sup>+</sup> embryo subjected to WIHC for pH3 (magenta), NF-kB activation (green), and the endothelial marker *kdrl* (red). The dashed circle indicates a mitotic pH3<sup>+</sup> cell. Notice that mitotic *kdrl*<sup>+</sup> ECs have inactive NF-kB (NF-kB<sup>-</sup>). The experiment was repeated three times independently with similar results. **D** Quantification of the percentage of pH3<sup>+</sup> cells from

(E, E', F, F'). Each dot represents 15–20 pooled embryonic trunks, *n* = 3. Black horizontal lines indicate mean ± SD. (E, F'') Representative histograms depicting flow cytometric analysis of 22hpf DMSO (E, E''), or 2 μM CAPE-treated (F, F''), dissociated *NF-kB:d2EGFP*<sup>+</sup>; *kdrl:mCherry*<sup>+</sup> embryonic trunks subjected to intracellular flow for d2EGFP, mCherry (blue), and pH3 (red). Chemical treatments were applied from 16hpf. E, F All *kdrl:mCherry*<sup>+</sup> cells. E', F' *kdrl:mCherry*<sup>+</sup>; *NF-kB:d2EGFP*<sup>+</sup> cells. E'', F'' *kdrl:mCherry*<sup>+</sup>; *NF-kB:d2EGFP*<sup>-</sup> cells. E''', F''' Representative contour plot of *kdrl:mCherry*<sup>+</sup>; *NF-kB:d2EGFP*<sup>+</sup> cells from (E''). The dotted line separates pH3<sup>-</sup> (left) from pH3<sup>+</sup> (right) cells. Data were analyzed by ordinary one-way ANOVA with Turkey's multiple comparisons test (B, D). Source data are provided as a Source Data file.

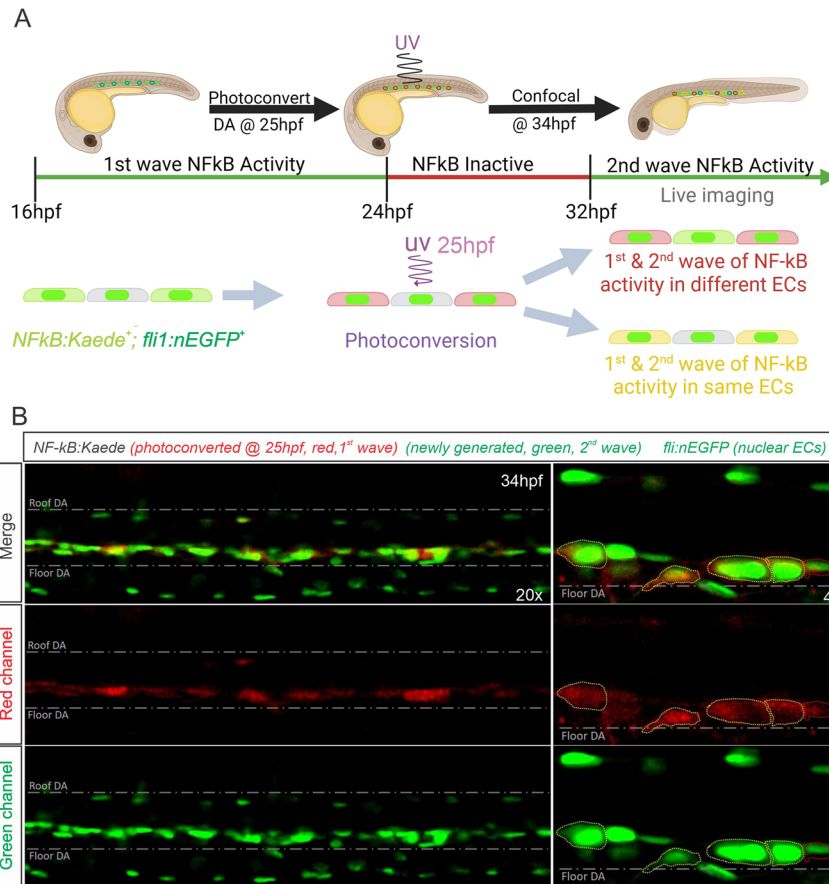


**Fig. 6 | In vivo NF-kB signaling dynamics at the single cell resolution.** **A** Illustration depicting the experimental design in (B). Briefly, *NFkB:Kaede*<sup>+</sup>; *fli1:nEGFP*<sup>+</sup> embryos were photoconverted at 25hpf with UV light for 10 min and subsequently subjected to confocal microscopy in the DA at 34hpf. **B** Representative maximum projection confocal images of the DA of 34hpf *NFkB:Kaede*<sup>+</sup>; *fli1:nEGFP*<sup>+</sup> embryos. Yellow (*Kaede* green<sup>+</sup>; *Kaede* red<sup>+</sup>) cytoplasm are

cells with both NF-kB activity waves occurring within the same cell (cells outlined in yellow). Dashed red delineates EC with *Kaede* (red<sup>+</sup>, green<sup>+</sup>) cytoplasm. The experiment was repeated three times independently with similar results. Figure 6A created with BioRender.com released under a Creative Commons Attribution-NonCommercial-NoDerivs 4.0 International license.

that Nod1, a microbial sensor that activates canonical NF-kB during bacterial infections<sup>94</sup>, primed ECs towards hemogenic<sup>40</sup>. Moreover, experiments using conditional p65 knockout mice crossed with Vav-Cre to deplete p65 in the hematopoietic compartment increased hematopoietic stem and progenitor cell cycling and hematopoietic lineage defects<sup>95</sup>, further supporting our results demonstrating that canonical NF-kB drives cell quiescence.

Additionally, our p65 chemical inhibition experiments after blood flow, together with previous work demonstrating high levels of p65 in budding HSPCs<sup>25</sup>, indicate that the second NF-kB activation wave could also be p65-dependent, and that the precise NF-kB activation and resolution is critical to drive the developmental progression of HSPCs. In future work, it would be interesting to assess whether p65

exerts its function by heterodimerizing with p50, as classically described<sup>96</sup>, or through other partners<sup>97</sup>. Future investigations to identify the direct transcriptional targets of p65 would also help close this knowledge gap.

At the molecular level, NF-kB signaling initiates after its release from inhibitor kappa B (IκB) in the cytosol, followed by translocation into the nucleus<sup>60</sup>. NF-kB activates IκB transcription, encompassing a delayed negative feedback loop that drives oscillations in NF-kB nuclear translocation while the stimulus is present<sup>98</sup>. These molecular oscillations, found in cell lines, have a typical period of ~100 min. In contrast, the in vivo NF-kB oscillatory kinetics identified in this work revealed the temporal activation of the NF-kB pathway during the entire HSPC developmental trajectory, which requires >20 h in the

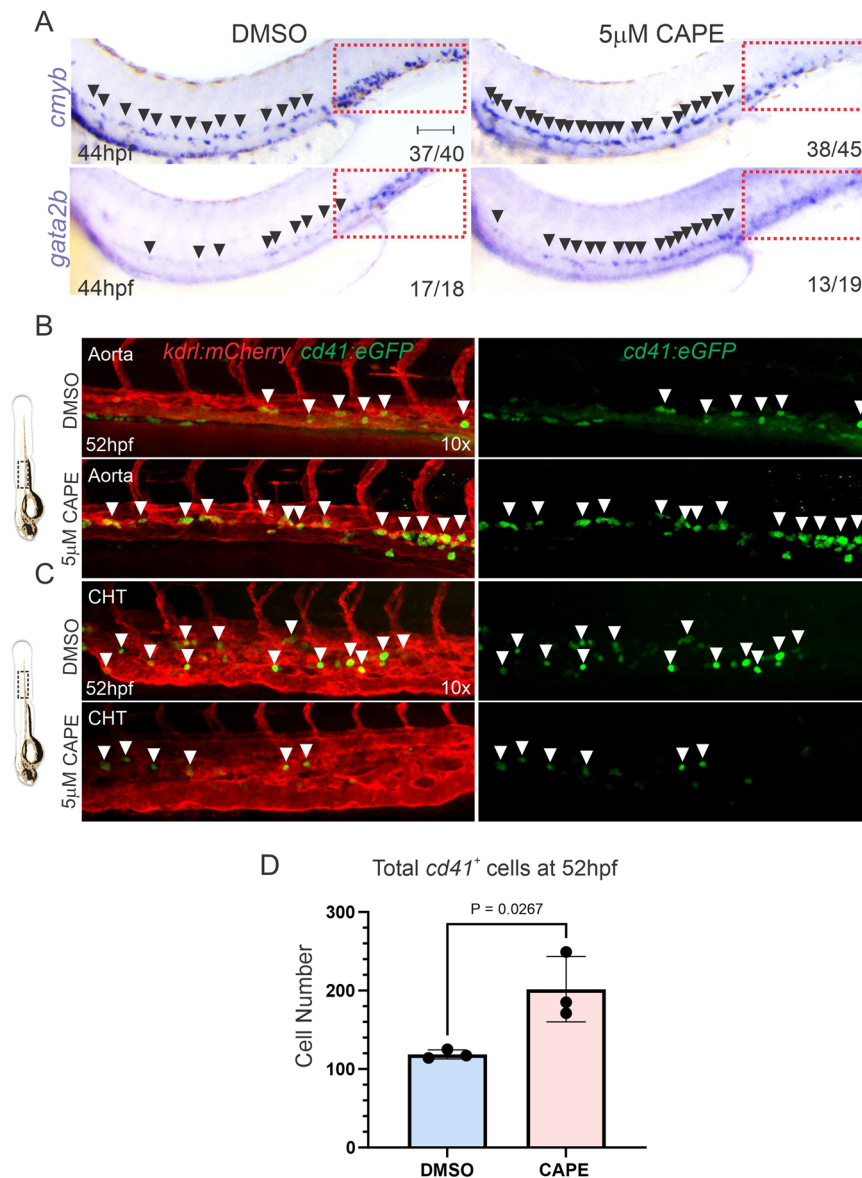


**Fig. 7 | Prolonged NF- $\kappa$ B resolution phase enhances the proliferative capabilities of nascent HSPCs.** **A** WISH for the HE markers *cmyb* and *gata2b* in 44hpf AB embryos treated with DMSO (left), or 5  $\mu$ M CAPE (right) from 28hpf. Red dashed boxes indicate the CHT region. Numbers in panels represent larvae with indicated phenotype. The experiment was repeated three times independently with similar results. **B**, **C** Representative confocal maximum projections of the DA (**B**), or CHT (**C**), from 52hpf *cd41:eGFP*<sup>+</sup>; *kdr1:mCherry*<sup>+</sup> embryos incubated with DMSO or 5  $\mu$ M

CAPE from 28hpf. White arrowheads indicate *cd41*<sup>+</sup> cells. Experiments were repeated three times independently with similar results. **D** Flow cytometric quantifications of total *cd41*<sup>+</sup> HSPCs from pooled 52hpf *cd41:eGFP*<sup>+</sup> embryos incubated with DMSO or 5  $\mu$ M CAPE from 28hpf. Each dot represents the total *cd41*<sup>+</sup> numbers within four pooled embryos. Black horizontal lines indicate mean  $\pm$  SD. Data were analyzed using an unpaired two-tailed *T*-test. Source data are provided as a Source Data file.

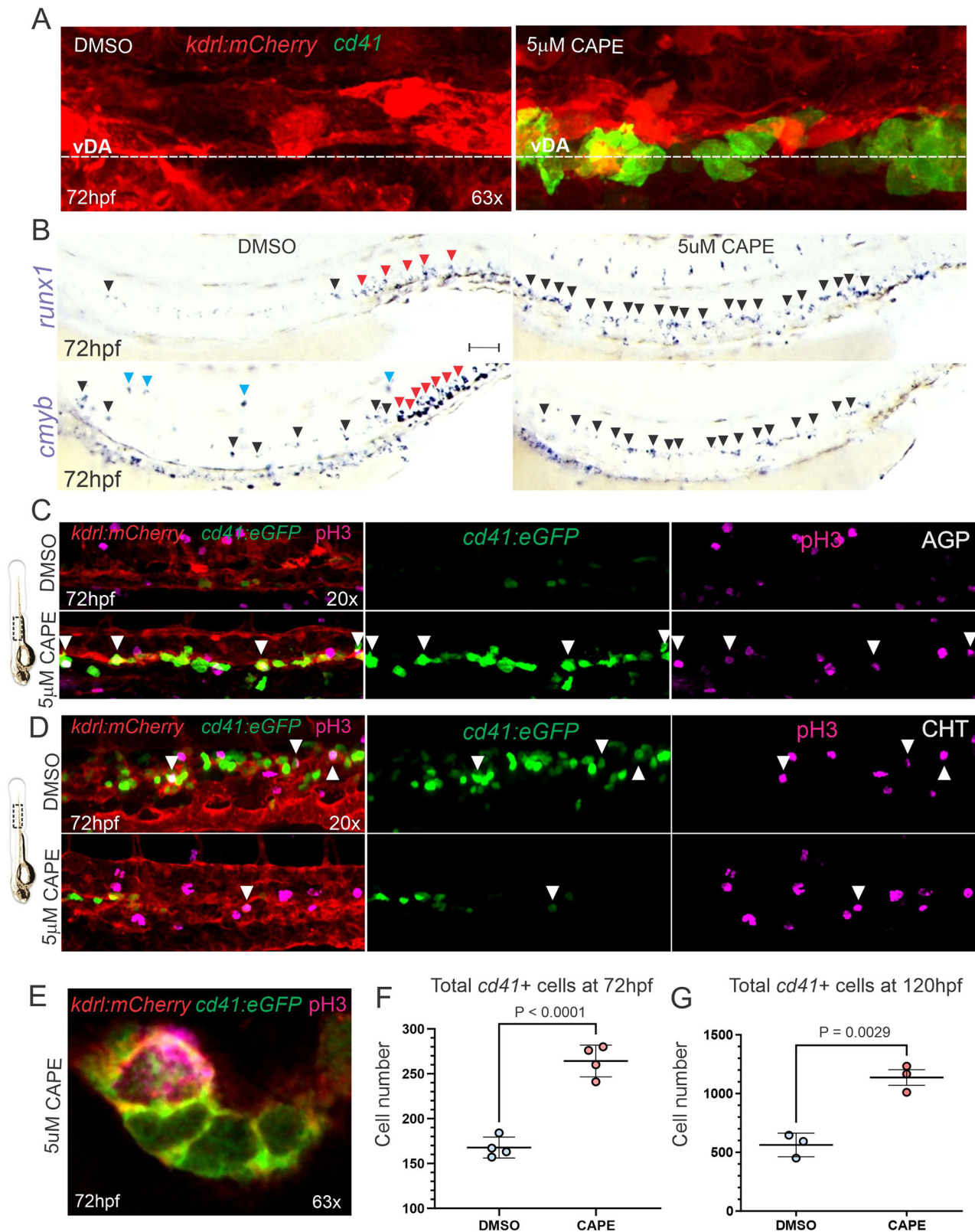
zebrafish. Whether the molecular oscillations of p65 between the nucleus and cytoplasm are part of the two NF- $\kappa$ B activity waves shown in this work would need further assessment.

In the last decade, a plethora of pro-inflammatory factors, most converging into NF- $\kappa$ B activation, have been identified to drive HSPC fate<sup>42–44</sup>. Our discovery here of a bimodal NF- $\kappa$ B activation sets up the stage to evaluate which factors could drive each independent NF- $\kappa$ B wave, and those necessary for the resolution of the pro-inflammatory program. Additionally, that hematopoietic transcription factors have been implicated in cell cycle, and that NF- $\kappa$ B inactivation correlates with their expression and the proliferative expansion of the HE, suggests that the shutdown of pro-inflammatory signaling and cell cycle re-entry is a prerequisite for the completion of the EHT. In agreement with our data, cell cycle progression has been proposed recently to be necessary to upregulate RUNX1C and differentiate ECs

into blood cells in a human system<sup>74</sup>, while neural crest cells specify in the G<sub>0</sub>/G<sub>1</sub> state<sup>99</sup>. In addition, we showed that the HSPC delamination from the DA is driven by NF- $\kappa$ B reactivation, and that this phenomenon occurs when cells are not proliferating. In agreement, cell delamination has been shown to occur when cells are in G<sub>1</sub> in other contexts<sup>100</sup>.

Assessing the effect of NF- $\kappa$ B signaling dynamics over particular HSPC populations, including erythroid, myeloid, or lymphoid-biased HSPCs, as well as multipotent progenitors, was outside of the scope of this work. Although currently, there is a lack of specific markers for these populations in zebrafish, experiments utilizing scRNAseq could help pinpoint the subtype of HSPC impacted by these dynamics. However, it is plausible that all these HSPC subtypes are impacted, since, in our work, we observed an almost total absence of HEC markers after p65 inhibition during early development.





The precise temporal identification *in vivo* of the first NF- $\kappa$ B activity requirement, and the impact on cell cycle regulation, has also been recapitulated in this work in a human system of definitive hematopoietic development<sup>77</sup>, supporting that our workflow outlined here to discover signaling dynamics is highly applicable to mechanisms of stem cell fate induction in upper vertebrates. By inhibiting NF- $\kappa$ B signaling in a very precise window of time with CAPE, an FDA-approved chemical, we have

been able to induce *in vivo* an expansion of nascent HSPCs to levels not seen before. While it was long assumed that HSPCs expanded in the fetal liver<sup>101</sup>, this notion has been recently challenged<sup>102</sup>, leaving the hematopoietic community puzzled on how to efficiently expand these clinically relevant stem cells. Progress in this area is provided in this study, in which we demonstrate that HSPCs can be expanded within the endothelial niche by prolonging the resolution of the inflammation phase.

**Fig. 8 | Proliferative HSPC clusters in vivo by prolongation of the pro-inflammatory resolution phase.** **A** Representative confocal maximum projections of the DA from 72hpf *cd41:eGFP<sup>+</sup>; kdrl:mCherry<sup>+</sup>* embryos incubated with DMSO (left) or 5  $\mu$ M CAPE (right) from 28hpf. The experiment was repeated four times independently with similar results. **B** WISH for the HE markers *runx1* (top) and *cmyb* (bottom) in 72hpf WT embryos treated with DMSO (left column) or 5  $\mu$ M CAPE (right column) from 28hpf. Black, red, and blue arrowheads denote HSPCs in floor of DA, CHT, and within the circulation, respectively. Scale bar = 100  $\mu$ M. The experiment was repeated three times independently with similar results. **C, D** Representative confocal maximum projections of the DA (**C**), or the CHT (**D**) from 72hpf *cd41:eGFP<sup>+</sup>; kdrl:mCherry<sup>+</sup>* embryos treated with DMSO (top) or 5  $\mu$ M CAPE (bottom) from 28hpf and stained for pH3. White arrowheads indicate *cd41<sup>+</sup>*

pH3<sup>+</sup> cells. Experiments were repeated three times independently with similar results. **E** Representative confocal maximum projection of a *cd41<sup>+</sup>*/pH3<sup>+</sup> cell within a *cd41<sup>+</sup>* cluster in the DA of a 72hpf *cd41:eGFP<sup>+</sup>; kdrl:mCherry<sup>+</sup>* embryos treated with 5  $\mu$ M CAPE from 28hpf. The experiment was repeated four times independently with similar results. **F** Flow cytometry quantification of HSPC (*cd41<sup>+</sup>*) numbers in pooled 72hpf *cd41:eGFP<sup>+</sup>; kdrl:mCherry<sup>+</sup>* embryos incubated with DMSO (blue) and 5  $\mu$ M CAPE (red) from 28hpf. Each dot represents four pooled embryos. Black horizontal lines indicate mean  $\pm$  SD. **G** Flow cytometry quantification of HSPC (*cd41<sup>low</sup>*) numbers in 120hpf *cd41:eGFP<sup>+</sup>; kdrl:mCherry<sup>+</sup>* embryos incubated with DMSO (blue) and 5  $\mu$ M CAPE (red) from 28–72hpf. Each dot represents four pooled embryos. Black horizontal lines indicate mean  $\pm$  SD. Data were analyzed using an unpaired two-tailed *T*-test (**F, G**). Source data are provided as a Source Data file.

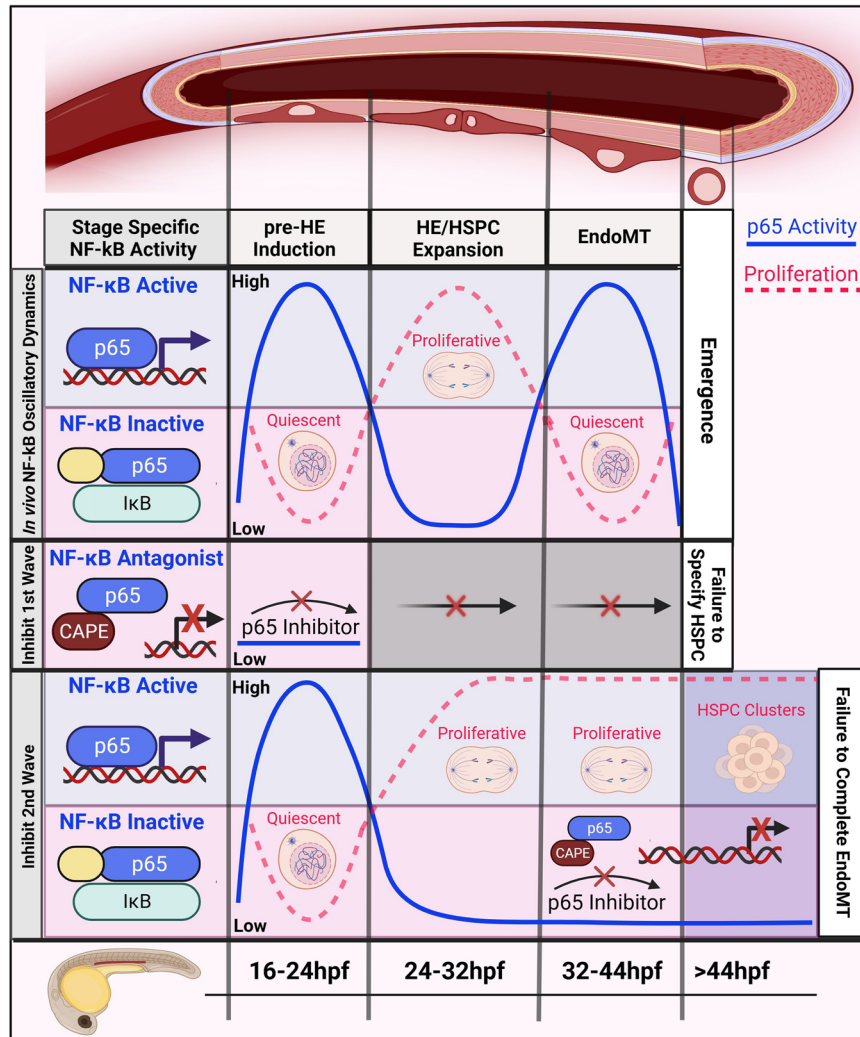


**Fig. 9 | Summary model of the temporal NF-κB (p65) regulation of HSPC development and cell cycle.** NF-κB activates within ECs to induce ECs to become hemogenic by restricting proliferation. NF-κB is subsequently inactivated, allowing for a proliferative expansion of the HE. Finally, NF-κB is re-activated in HECs to drive EndoMT. When the first NF-κB activity wave is disrupted, HE fails to specify. In

contrast, disruption of the second wave of NF-κB activity leads to continued proliferation of the HE pool, preventing their delamination from the DA. Figure 9 created with BioRender.com released under a Creative Commons Attribution-NonCommercial-NoDerivs 4.0 International license.

**Methods**

**Ethics declarations and approval for animal experiments**

The zebrafish research in this study was performed according to the Guidelines for Ethical Conduct in the Care and Use of Animals<sup>103</sup>. All zebrafish experiments were performed according to Iowa State University Animal Care and Use Committee IACUC-20-025 and IACUC-20-024 approved protocols, and in compliance with ARRIVE guidelines<sup>104</sup>,

and the American Veterinary Medical Association (2020) and NIH guidelines for the humane use of animals in research.

**Zebrafish husbandry and strains**

Zebrafish (*Danio rerio*) embryos and adults were mated, staged, raised, and processed as described<sup>105</sup> in a circulating aquarium system maintained at 26 °C on a 14 hr light/10 h dark cycle. Zebrafish lines used in

this study were: WT AB (ZDB-GENO-960809-7, *Zebrafish International Resource Center, ZIRC*, <https://zebrafish.org/home/guide.php>), transgenic *Tg(kdrl:HsHRAS-mCherry)<sup>ts96</sup>* (referred to as *kdrl:mCherry* throughout the manuscript)<sup>35</sup>, *Tg(-6.0itga2b:eGFP)<sup>ts2</sup>* (referred to as *cd41:eGFP* throughout the manuscript)<sup>106</sup>, *Tg(lmo2:eGFP)<sup>ts72 107</sup>*, *Tg(gata1:DsRed)<sup>ts2 108</sup>*, *Tg(fli1:nEGFP)<sup>ts780</sup>* (*Zebrafish International Resource Center, ID: ZL1363*), *TgBAC(runx1P2:Citrine)<sup>ts788 37</sup>*, *Tg(NFKB:eGFP)<sup>ts45</sup>*, *Tg(NFKB:d2EGFP)<sup>ts502</sup>* (this work), *Tg(NFKB:d2mRFP)<sup>ts503</sup>* (this work), *Tg(NFKB:Kaede)<sup>ts504</sup>* (this work), and various intercrosses of these lines were utilized.

### Morpholino injection

Std-MO (5'-CCTCTTACCTCAGTTACAATTTATA-3') (Gene Tools) and p65-MO (5'- CCCACTGGTGAACATTCGGTCCAT-3')<sup>109</sup> were resuspended in nuclease-free water at a stock concentration of 2 mM. A mix containing 1  $\mu$ l of phenol red solution (Sigma, P0290), 2  $\mu$ l of MO (2  $\mu$ M), and 2  $\mu$ l of nuclease-free water (Fisher Scientific, BP2484100) was prepared as a working solution, and 520  $\mu$ l (0.8  $\mu$ M final MO concentration) injected into 1–2 cell stage embryos using PLI-90A pico-injector warner instruments.

### Generation of *Tg(6xHsa.NFKB:d2EGFP)<sup>ts502</sup>*, *Tg(6xHsa.NFKB:d2mRFP1)<sup>ts503</sup>*, and *Tg(6xHsa.NFKB:Kaede)<sup>ts504</sup>* zebrafish

The pNfkb:eGFP was a gift from John Rawls<sup>45</sup> (Addgene plasmid #44922; <http://n2t.net/addgene:44922>; RRID:Addgene\_44922). The eGFP from pNfkb:eGFP backbone was excised using ClaI (R0197S, NEB) and NcoI-HF (R3193S, NEB) following the manufacturers' instructions. The pNfkb:eGFP backbone lacking eGFP was purified using Monarch<sup>®</sup> PCR & DNA Cleanup Kit (TI030L). The destabilized version of eGFP (d<sub>2</sub>eGFP) was amplified from pScel Dusp6:d2EGFP (a gift from Michael Tsang; Addgene plasmid # 32667; <http://n2t.net/addgene:32667>; RRID:Addgene\_32667)<sup>48</sup> by PCR using Q5<sup>®</sup> High-Fidelity DNA Polymerase (NEB #M0491S) (annealing temperature: 62.5 °C, 18 cycles). mRFP1 was amplified from pDB790 Tol2/gCry:GFP, 14XUAS:mRFP<sup>110</sup>, available from the lab of Dariusz Balciunas, Temple University, by PCR using Q5<sup>®</sup> High-Fidelity DNA Polymerase (NEB #M0491S) (annealing temperature: 65 °C, 18 cycles). Kaede was amplified from pME-Kaede (gift from Nathan Lawson; Addgene plasmid # 132972; <http://n2t.net/addgene:132972>; RRID:Addgene\_132972) by PCR using Q5<sup>®</sup> High-Fidelity DNA Polymerase (NEB #M0491S) (annealing temperature: 60 °C, 18 cycles). Primers are specified in Table S1. In d2EGFP and d2mRFP1, eGFP and mRFP1, respectively, were destabilized by residues 422–461 of mouse ornithine decarboxylase, giving an in vivo half-life of ~2 h<sup>48</sup>.

The NEBuilder<sup>®</sup> HiFi DNA Assembly Cloning Kit (NEB #E5520) was utilized to subclone the PCR-amplified d2EGFP (3:1 ratio insert:vector), mRFP1 (2:1 ratio insert:vector) and PEST sequence (5:1 ratio insert:vector) into the pNfkb backbone. A total volume of 520  $\mu$ l containing 40–50 ng/ $\mu$ l transposase mRNA and 50–150 ng/ $\mu$ l of the correspondent plasmid DNA was injected into the one-cell stage AB embryos using Narishige One Axis Oil Hydraulic Micromanipulator No: MMO220 C and Picospritzer II (Parker Hannifin). At 24 hpf, embryos were dechorionated by hand, sorted based on fluorescent expression resembling NF- $\kappa$ B activity patterns<sup>45</sup>, and raised to adulthood. Potential F<sub>0</sub> founders were in-crossed to identify transmitters. We identified one founder line that exhibited strong d2EGFP, d2mRFP1, or Kaede expression within regions of known NF- $\kappa$ B activity in the developing embryo<sup>45</sup>. These founders were outcrossed with AB WT fish, and the subsequent F<sub>2</sub>-F<sub>6</sub> progeny of the *Tg(6xHsa.NFKB:d2EGFP)<sup>ts502</sup>*, called *Tg(NFKB:d2EGFP)<sup>ts502</sup>*, *Tg(6xHsa.NFKB:d2mRFP1)<sup>ts503</sup>*, called *Tg(NFKB:D2mRFP)<sup>ts503</sup>*; and *Tg(6xHsa.NFKB:Kaede)<sup>ts504</sup>*, called *Tg(NFKB:Kaede)<sup>ts504</sup>*, throughout this manuscript, used for the experiments outlined in this work.

### *rela* (p65) gRNA target site design, Cas9:gRNA complex and CRISPRant generation

CRISPRScan (<http://www.crisprscan.org/>) and IDT websites were used to identify and order the *rela* synthetic gRNA 5'-AAGTGTGAGGGTC-GATCGGC-3' located in exon 3 of zebrafish *rela* (ensembl ENSDARGO0000098696 and ENSDARTO0000159359.3 *rela*-201). Functional Cas9:gRNA complexes were generated by incubating Cas9 protein with an equimolar amount of gRNA at a final concentration of 10  $\mu$ M each. About 62  $\mu$ M stock solution of Cas9 protein (IDT, Alt-R S.p. Cas9 Nuclease v3, 100  $\mu$ g, Cat No:1081058) in nuclease-free duplex buffer (IDT Cat No:1072570) was stored at -80 °C. About 1  $\mu$ l of 50  $\mu$ M sgRNA was gently mixed with 0.81  $\mu$ l of 62  $\mu$ M Cas9 protein stock and 1  $\mu$ l of duplex buffer. Prior to microinjection, the complex solution was incubated at 37 °C for 5 min and placed on ice. Two nanoliters (2 nl) of Cas9:gRNA complex was injected into the cytoplasm of one-cell stage zebrafish embryos. To confirm gRNA editing and mutagenesis efficiency, genomic DNA was extracted from individual 24 hpf injected embryos by incubation in 25  $\mu$ l NaOH at 95 °C for 30' followed by the addition of 2.5  $\mu$ l 1 M Tris pH 7.5. About 2  $\mu$ l of genomic DNA was used for PCR amplification with *rela* forward primer exon2F 5'-GAACTTCGACAGGTGCCTCA-3' and reverse primer intron3R 5'-GCAG-TAAGCGTCAGAGGTGT-3'. PCR products were analyzed by gel electrophoresis or purified using the Qiagen PCR purification kit (Qiagen 28104). Purified PCR amplicons were Sanger sequenced and analyzed for indel efficiency using Synthego's Inference of CRISPR Edits (ICE) analysis software (<https://ice.synthego.com/#/>).

### *p65<sup>stop</sup>* knockin allele generated by GeneWeld CRISPR-Cas9 targeted integration

The GeneWeld targeted integration donor vector pPRISM(UgRNA-3XStop; myl7:mRFP-UgRNA)<sup>64</sup> (Addgene #117772) was modified by replacement of the *myl7* promoter with a hatching gland-specific *he1a* promoter<sup>111</sup> using HiFi Cloning (NEB E5520S) to build *pPRISM(UgRNA-3XStop; he1a:mRFP-UgRNA)*. CRISPR/Cas9 targeted integration of the *3XStop-he1a:mRFP* cassette into p65 (*rela*) exon 3 to isolate a loss of function allele was performed as described previously<sup>62–64</sup>. Briefly, 48 bp homology arms complementary to sequences 5' and 3' to the *rela* exon 3 genomic CRISPR/Cas9 gRNA cut site (Table S1) were cloned into *BfuAI* and *BspQI* type IIS restriction enzyme sites flanking the *3XStop; he1a:mRFP* cassette to build the donor vector *rela-Stop-he1a:mRFP*. 5'-capped Cas9 mRNA was in vitro transcribed from pT3TS-nCas9n expression vector (Addgene #46757)<sup>112</sup> linearized with *XbaI* (New England Biolabs, R0145S). About 1  $\mu$ g linearized vector was purified with the PureYield Plasmid Miniprep System (Promega, A1223) and used as a template for in vitro synthesis using Ambion mMessage Machine T3 Transcription Kit (Thermo Fisher, AM1348). In vitro synthesized mRNA was purified with the RNA Clean and Concentrator Kit RCC (Zymo, R1013). One-cell stage WIK wild-type embryos were co-injected with 2 nl of a solution containing 25 pg *rela* exon 3 genomic gRNA, 25 pg UgRNA, 10 pg *rela-Stop:he1a:mRFP* targeting vector, and 300 pg Cas9 mRNA. About 50 injected embryos showing hatching gland mRFP expression were raised to adulthood, and adults were screened for transmission of hatching gland-specific mRFP expression to the F1 generation. At least 75 embryos were screened from each cross. From 18 adults, two founders were identified, one transmitting a precise integration allele with expected 5' and 3' junctions (Fig. S5), and the other allele had only a precise 3' junction. Hatching gland mRFP positive embryos carrying a precise *rela-Stop:he1a:mRFP* integration allele were identified by 5' and 3' PCR junction analysis and Sanger sequencing. Sibling F1 mRFP positive embryos were raised to adulthood and confirmed by fin clip 5' and 3' PCR junction analysis and Sanger sequencing. A single confirmed F1 adult was outcrossed to WIK, and a single confirmed F2 adult was outcrossed to WIK to establish transgenic line *Tg(rela-3XStop; he1a:mRFP)<sup>ts67</sup>*.



### Zebrafish chemical treatments

Twenty-five zebrafish embryos were incubated in Petri dishes with 25 ml of E3 water (ZFIN) and 0.003% 1-phenyl 2-thiourea (PTU) containing 2 or 5  $\mu\text{M}$  of Caffeic Acid phenylethyl ester (CAPE) (Cayman chemical #70750)<sup>49</sup> at the specified developmental times. Control embryos were incubated with 0.1  $\mu\text{M}$  DMSO. To prepare the CAPE stock solution, 100 mg of CAPE were dissolved in 3 ml of DMSO and heated at 55 °C for 5 min.

### Quantitative RT-PCR analysis

mRNA was purified from FACS-sorted cells using RNeasy Micro Kit (Qiagen), and cDNA was generated with iScript gDNA Clear cDNA Synthesis Kit (BioRad). Primers to detect zebrafish transcripts are described in Table S1. qPCR was performed with CFX Connect Real-Time PCR System (BioRad CFX Maestro 2.0, v5.0.021.0616). Analysis was conducted as previously described in ref. 113.

### Detection of apoptotic cell death by TUNEL labeling

The TUNEL assay was performed as previously described<sup>25</sup> using Streptavidin-647 (S21374; Thermo Fisher), anti-eGFP antibody (GFP-1010; Aves), and DAPI 1:1000 (D1306; Invitrogen) (Table S2). Embryos were subsequently imaged in a Zeiss LSM 700 Laser Scanning Confocal with Zen Black software (v14.0.27.701). Apoptotic cells were counted manually throughout the confocal planes.

### Kaede photoconversion

24 hpf *fli1:nEGFP<sup>+</sup>; Nfkb:Kaede<sup>+</sup>* embryos were dechorionated with pronase (I1459643001, Sigma) and anesthetized in 1% tricaine (Pentair; TRS5). 25 hpf single embryos were exposed in glass plates (WillCo-dishKIT, KIT-5040#1.5; WILLCOWELLS BV) for 10 min to UV light in a Leica M205 FCA to induce kaede photoconversion from green (518 nm) to red (572 nm) fluorescent emission. At 34 hpf, embryonic trunks were imaged with a Zeiss LSM 700 Laser Scanning Confocal with Zen Black software (v14.0.27.201).

### Flow cytometric analysis

Quantification of *Nfkb:d2EGFP<sup>+</sup>, kdrl:mCherry<sup>+</sup>* and *cd41:eGFP<sup>+</sup>, kdrl:mCherry<sup>+</sup>* embryos at their indicated treatment and developmental stage entailed ~20–25 pooled embryos that were dechorionated with pronase (MilliporeSigma; I1459643001) and anesthetized in 1% tricaine (Pentair; TRS5) as previously described<sup>66</sup>. The trunk region of each embryo was surgically isolated (posterior to the yolk ball and anterior to the urogenital canal) using scalpel blades (RS-9801-15, Roboz Surgical Store). The collected tissue was then gently vortexed at 28.5 °C for 5–20 min with 50  $\mu\text{g}/\text{ml}$  Liberase TM (MilliporeSigma; REF: 5401127001) in Dulbecco's Phosphate Buffered Saline solution with  $\text{Ca}^{2+}$  and  $\text{Mg}^{2+}$  (MilliporeSigma, D8662). The resulting cell suspension was filtered through a 30  $\mu\text{m}$  nylon mesh (Fisher Scientific; NC9084441) using a 21-gauge syringe (Fisher Scientific; BD 309624) and stained with SYTOX<sup>™</sup> Red (Life Technologies; S34859) to exclude dead cells. Flow cytometric acquisitions were performed on a Melody (BD) with FACSCorus 2.0, version 1.1.20.0 software, and analyses using FlowJo software (v10.3 or v10.8.1, Tree Star). To quantify total *cd41:eGFP<sup>+</sup>* cells in 96 hpf larvae, five whole larvae were pooled for each indicated treatment and processed as described above.

### FACS sorting, RNA sequencing (RNA-seq), and library preparation

22 hpf *Nfkb:d2EGFP x kdrl:mCherry* zebrafish embryos were screened with Leica M165FC stereomicroscope, dechorionated with pronase (MilliporeSigma; I1459643001), anesthetized in 1% tricaine (Pentair; TRS5) and dissociated as described above (see above flow cytometric analysis and ref. 66). *kdrl<sup>+</sup>/Nfkb<sup>-</sup>* and *kdrl<sup>+</sup>/Nfkb<sup>+</sup>* cells were each

sorted and collected with BD FACS Aria III. Each condition was performed in triplicate, with ~7000 sorted cells per sample. FACS-sorted cells were collected in Eppendorf tubes containing 250  $\mu\text{l}$  of RLT buffer. RNA was then isolated and purified with RNeasy<sup>®</sup> Micro Kit (Qiagen). DNase I treatment was performed as specified by the manufacturer. Total RNA was assessed for quality and quantity using an Agilent 2100 Bioanalyzer with RNA 6000 Pico Kit. Triplicate RNA samples of each condition were processed following the manufacturer's instructions. Samples were then used to generate RNA sequencing libraries using NEBNext Single Cell/Low Input RNA Library Prep Kit (NEB #E6420S/L) for Illumina and NEB's Unique Dual Index primers for Illumina (E6440). Resulting libraries were multiplexed and sequenced with 100 basepair (bp) single reads (SR75) to a depth of approximately 20 million reads per sample on a NovaSeq SP.

### RNA-seq data analysis

The raw RNA-seq data generated in this study has been deposited in the NCBI GEO database with accession number GSE253758. The majority of results were produced in a ROSALIND<sup>®</sup> (<https://rosalind.bio/>) analysis, with a HyperScale architecture developed by ROSALIND, Inc. (San Diego, CA). Supplementary Data File 1 indicates all genes detected, their fold increase, and p-adjusted value, as normalized reads. Reads were trimmed using cutadapt v1.11, and requiring a minimum read length 17. Quality scores were assessed using FastQC v0.11.3 (<https://www.bioinformatics.babraham.ac.uk/projects/fastqc/>). Reads were aligned to the *Danio rerio* genome build danRer10 using STAR v2.4.2a<sup>114</sup> with option --outSAMstrandField intronMotif. Individual sample reads were quantified using HTseq v0.6.0<sup>115</sup> with option -s no. Counts were normalized via CPM and size factors for visualizations using DESeq2 R library v1.14.1<sup>116</sup>. Read distribution percentages, violin plots, identity heatmaps, and sample MDS plots were generated as part of the QC step using RSeQC v2.6.4<sup>117</sup>. DESeq2 was also used to calculate fold changes and *p* values. The clustering of genes for the final heat map of differentially expressed genes was done using the PAM (Partitioning Around Medoids) method from the fpc R library v2.2-5. The hypergeometric distribution was used to analyze the enrichment of pathways, gene ontology, domain structure, and other ontologies. The topGO R library, was used to determine local similarities and dependencies between GO terms in order to perform Elim pruning correction. Several database sources were referenced for enrichment analysis, including Interpro, NCBI, MSigDB, REACTOME, and WikiPathways]. Enrichment was calculated relative to a set of background genes relevant to the experiment. Because *relb* was missing from the ROSALIND annotation due to their use of *danRer10*, we repeated the analysis with *danRer11*. We used Flexbar v3.5.0 (Dodt2012) for two rounds of adapter trimming, the first (--adapter-preset TruSeq --adapter-trim-end RIGHT --adapter-min-overlap 5 --min-read-length 15) to remove TruSeq adapters and the second (--max-uncalled 3 --adapter-trim-end LEFT --adapter-revcomp ON --adapter-revcomp-end RIGHT --adapter-min-overlap 5 --htrim-left GT --htrim-right CA --htrim-min-length 1 --htrim-error-rate 0.01 --min-read-length 15 and a custom adapters file) to trim the TSO plus polyG and RT primer plus polyA used in the NEBNext kit. The reads were aligned to danRer10 by STAR v2.7.11b and quantified by HTSeq v2.0.5, using the same options as ROSALIND. The counts were loaded into R v4.3.3 library DESeq2 v1.42.0, normalized using function rlog() with option blind=FALSE for visualization, and analyzed for differential expression. Adjusted *p* values are the defaults reported by DESeq2 function results. The results are highly correlated with the ROSALIND results. For the 2473 genes with an adjusted *p* value below 0.001 in the ROSALIND results, 2458 were in our data. For these genes, the Pearson correlation of log<sub>2</sub> fold change between ROSALIND and our results exceeded 0.98 for all six samples. For the subset of these genes (size 1963) with positive adjusted *p* values by both pipelines, the Pearson correlation in log adjusted *p* values was over 0.96. Our results were used for Fig. 2B to include *relb*.

### Cleavage under targets and release using nuclease (CUT&RUN)-qPCR

To validate the specific inhibitory activity of CAPE over the zebrafish ortholog p65, CUT&RUN-qPCR was performed as previously described<sup>166,118</sup> using the CUT&RUN Assay Kit (Cell Signaling; 86652). Fifty 23hpf AB<sup>+</sup> zebrafish embryos were dissociated and pooled per sample. ~100,000 cells per sample, and three samples per condition were analyzed. About 5  $\mu$ l (dilution 1:20) of IgG isotype control antibody (Cell Signaling, #66362), and 4  $\mu$ l of p65 antibody (dilution 1:25) (Thermo Fisher, PA5-16545) were used per sample. DNA purification was carried by phenol/chloroform as indicated by the manufacturer (Cell signaling, 86652S), and qPCR analysis of the predicted p65 binding sites (BSs) using the following primers: BS1 (+830), BS2 (+895), BS3 (+1002), BS4 (+3078), and BS5 (+3264) (Table S1). As control loci, we selected two fragments located at -5717 (control BS1) and +5697 (control BS2) from *nfkbiaa*, since they didn't show any predicted binding sites for p65<sup>66</sup>, and performed qPCR using the primers described in Table S1. To calculate the fold enrichment, qPCR results for each BS were normalized against the input and IgG control as described by the CUT&RUN Assay Kit #86652 (Cell Signaling), and internal control gene (*tert*).

### Whole-mount immunohistochemistry (WIHC)

WIHC was performed as previously described in ref. 119. The following antibodies were used (Table S2): rabbit anti-phospho-Histone H3 (Ser10) antibody (Cell Signaling, 9701S) (dilution 1:400), rabbit anti-Mfap4 (Genetex, GTX132692) (dilution 1:100), chicken anti-GFP IgY antibody (Aves Labs GFP-1020) (dilution 1:200), mouse anti-mCherry (Clontech, 632543), goat anti-Chicken IgY (H+L) Alexa-488 (Life Technologies, A-11039) (dilution 1:500), goat anti-mouse IgG (H+L) Alexa-594 (Life Technologies, A11032) (dilution 1:500), goat anti-Rabbit IgG (H+L) Alexa-647 (Life Technologies, A21245) (dilution 1:500). The samples were imaged with Zeiss LSM 700 Laser Scanning Confocal with Zen Black (v14.0.27.201) software.

### Whole-mount RNA in situ hybridization (WISH)

WISH was performed as described in ref. 120. Probes used for *cmyb*, *runx1*, *mpx*, *mpeg*, *l-plastin* *gata1*, and *kdrl* transcripts were generated from linearized plasmids using the DIG RNA Labeling Kit (MilliporeSigma; 11175025910). Embryos were imaged using a Leica M165FC stereomicroscope equipped with a DFC295 color digital camera (Leica) and FireCam software (Leica) with Leica Application Suite X (v3.7.0.20979). Embryos assessed by WISH for *runx1* and *cmyb* were manually counted to enumerate HSPCs. Zebrafish embryos assessed by WISH for *runx1*, *cmyb*, *mpx*, *mpeg*, and *l-plastin* at noted stages cells were imaged and manually counted. For WISH analysis of *cmyb* on the *p65*<sup>STOP</sup> lof allele, *p65*<sup>STOP/+</sup> heterozygous were incrossed, and the progeny subjected to WISH for *cmyb* at 44hpf. Embryos were imaged in PBT and individually genotyped using the primers specified in Table S1 using a three-primer allele-specific diagnosis. Briefly, WT p65 allele band size was 639 bp in *p65*<sup>+/+</sup> and *p65*<sup>STOP/+</sup> embryos. The targeted integrated p65 allele band size was 753 bp in *p65*<sup>STOP/STOP</sup> and *p65*<sup>STOP/+</sup> embryos. A "Touch Down" function was performed with an annealing temperature of 58 °C (-0.5 °C for 16 cycles). The second annealing was at 50 °C for 38 cycles total. About 20  $\mu$ l of the reaction was run on an agarose gel for diagnostics. The pictures taken from each embryo were then clustered based on the three genotypes obtained (*p65*<sup>+/+</sup>, *p65*<sup>STOP/+</sup>, *p65*<sup>STOP/STOP</sup>).

### Fluorescent visualization of apoptotic cells, *Tg(NFkB:D2EGFP)*, *Tg(kdrl:mCherry)*, and *Tg(Cd41:eGFP)* embryos

Fluorescent images of TUNEL-subjected embryos and live transgenic embryos were taken at the mentioned stages using the appropriate

filters in a Leica M205 FCA stereomicroscope equipped with a THUNDER imager, or EVOS M5000 microscope. Live embryos were anesthetized in 1% tricaine (Pentair; TR55).

### Confocal time-lapse imaging of transgenic zebrafish embryos

*NFKB:d2EGFP*; *kdrl:mCherry* zebrafish embryos were screened with Leica M165FC stereomicroscope, manually dechorionated, anesthetized in 1% tricaine (Pentair; TR55), mounted in low melting agarose containing tricaine anesthetic and imaged using a Zeiss LSM 700 confocal microscope. D<sub>2</sub>EGFP and mCherry were excited by 488 and 594 nm laser lines, respectively. z-stacks were taken every 3 to 5 min. Movies were created with Zen Black (v14.0.27.201) software.

### Cell cycle analysis of embryonic endothelial cells

*Kdrl:mCherry* and *NFKB:d2EGFP* transgenic zebrafish embryos at the indicated stages were dissociated as previously described with the exception of Hanks' Balanced Salt Solution (HBSS) (Sigma, H826) in replace of PBS, and HBSS with Ca<sup>2+</sup>, Mg<sup>2+</sup> (Sigma, H6648) in replace of PBS with Ca<sup>2+</sup>, Mg<sup>2+</sup><sup>66</sup>. Dissociated embryonic cells were stained with Vibrant DyeCycle Ruby Stain (Thermo Fisher, Cat# V10309) following the manufacturer's recommendations, except for the incubation temperature, which was carried at 28.5 °C.

### Pluripotent stem cells differentiation to human hematopoietic progenitors

Three independent iPSC lines were used in this study: FL24.9, FL24.24<sup>121</sup>, and CHOPWT6 (Bone marrow-derived iPSC line)<sup>122</sup>. iPSCs were differentiated as previously described in refs. 40,77 with minor modifications. Briefly, EBs were generated from iPSCs using an orbital shaker at 80 rpm under 5% CO<sub>2</sub> and 5% O<sub>2</sub> at 37 °C for 30 h. Subsequently, differentiation was induced by SFD media supplemented with 10 ng/ml BMP4. Mesoderm was induced 1.75 days later by 3  $\mu$ M CHIR99021 (Tocris) and 6  $\mu$ M SB431542 (Cayman Chemicals). At day 4, the medium was changed to StemPro34 (Invitrogen) with 15 ng/ml recombinant human VEGF and 5 ng/ml bFGF (R&D Systems). At day 6, cultures were fed on top with 15 ng/ml VEGF, 5 ng/ml bFGF, 100 ng/ml SCF, 50 ng/ml IGF1 (R&D Systems), and 5  $\mu$ M of retinol (Sigma). About 5  $\mu$ M of CAPE (Cayman Chemicals), or an equivalent volume of DMSO control was added on the specified days. EBs were dissociated using Collagenase B (Roche) at day 9 and stained with CD34, CD43, CD184, and CD73 antibodies. About 12,000 sorted cells were reaggregated overnight in low attachment 96-well U-bottom plates in StemPro34 with 5 ng/ml VEGF, 30 ng/ml TPO, 30 ng/ml IL-3, 10 ng/ml FLT3L, 100 ng/ml SCF, 25 ng/ml IGF1, 5 ng/ml bFGF, 20 ng/ml SHH, and 10 ng/ml BMP4. Aggregates were transferred the next day onto GFR Matrigel-coated six-well plates. Every 3 days, the wells were fed on top with StemPro34 containing 30 ng/ml TPO, 10 ng/ml IL-3, 5 ng/ml FLT3L, 100 ng/ml SCF, and 25 ng/ml IGF1.

### Generation of human definitive hemogenic endothelium from iPSCs

For RUNX1 intracellular staining, day 9 EBs were dissociated and single cells were fixed in PBS 1.6% PFA for 10 min at RT under gentle agitation and washed with PBS. Cells were permeabilized, washed, and stained with Intracellular Staining Permeabilization Wash Buffer (Biologend) as previously described in ref. 40.

### Cell cycle analysis in differentiated iPSCs

EBs were dissociated to single cells using Collagenase B (Roche) and washed with PBS 2% BSA. Cells were stained with Alexa Fluor<sup>®</sup> 488 anti-human CD34 Antibody (BioLegend, 343518, 1:50) for 30 min at RT in the dark. Cells were washed 2x with PBS 2% BSA and pelleted at 500 $\times$ g for 3 min. While vortexing, 3 ml of ice-cold methanol was added to the

cell pellet, and the tubes were incubated at  $-20^{\circ}\text{C}$  for 1 h. Cells were pelleted and washed 2x with 1 ml of PBS 2% BSA. Cells were stained with Ki67 antibody (BioLegend #350514, APC-conjugated, 1:100) at RT in the dark for 30 min. After washing, cells were resuspended in PBS 2% BSA, and FxCycle Violet (Invitrogen#F10347) was added according to manufacturer instructions. Single stained controls were performed, together with a cell cycle inhibitor control.

### Statistical analyses

Two to three independent experiments were performed per experiment type. Statistical analysis and data representation were performed with Graphpad Prism 5 or Graphpad Prism 9. Data were analyzed by unpaired two-tailed *t*-test and confidence intervals at 95%, or ordinary one-way ANOVA with Tukey's test and confidence intervals at 95%. In all figures, the middle black bars denote the mean and the error bars represent SD.

### Reporting summary

Further information on research design is available in the Nature Portfolio Reporting Summary linked to this article.

### Data availability

For the human iPSCs-derived dataset, gene expression values were obtained from the website (<https://lab.antonellafidanza.com/>) in Supplementary Fig. 13. The raw RNA-seq data generated in this study has been deposited in the NCBI GEO database with accession number [GSE253758](https://www.ncbi.nlm.nih.gov/geo/query/acc.cgi?acc=GSE253758). All data generated in this study are available in the Article and Supplementary Information. Source data are provided with this paper.

### References

- Takahashi, K. & Yamanaka, S. Induction of pluripotent stem cells from mouse embryonic and adult fibroblast cultures by defined factors. *Cell* **126**, 663–676 (2006).
- Clements, W. K. et al. A somitic Wnt16/Notch pathway specifies haematopoietic stem cells. *Nature* **474**, 220–224 (2011).
- Grainger, S. et al. Wnt9a is required for the aortic amplification of nascent hematopoietic stem cells. *Cell Rep.* **17**, 1595–1606 (2016).
- Goessling, W. et al. Genetic interaction of PGE2 and Wnt signaling regulates developmental specification of stem cells and regeneration. *Cell* **136**, 1136–1147 (2009).
- Richter, J., Traver, D. & Willert, K. The role of Wnt signaling in hematopoietic stem cell development. *Crit. Rev. Biochem. Mol. Biol.* **52**, 414–424 (2017).
- Thambyrajah, R. & Bigas, A. Notch signaling in HSC emergence: when, why and how. *Cells* **11**, 358 (2022).
- Imanirad, P. et al. HIF1 $\alpha$  is a regulator of hematopoietic progenitor and stem cell development in hypoxic sites of the mouse embryo. *Stem Cell Res.* **12**, 24–35 (2014).
- Gerri, C., Marass, M., Rossi, A. & Stainier, D. Y. R. Hif-1 $\alpha$  and Hif-2 $\alpha$  regulate hemogenic endothelium and hematopoietic stem cell formation in zebrafish. *Blood* **131**, 963–973 (2018).
- Monteiro, R. et al. Transforming growth factor beta drives hemogenic endothelium programming and the transition to hematopoietic stem cells. *Dev. Cell* **38**, 358–370 (2016).
- Chanda, B., Ditadi, A., Iscove, N. N. & Keller, G. Retinoic acid signaling is essential for embryonic hematopoietic stem cell development. *Cell* **155**, 215–227 (2013).
- Dou, D. R. et al. Medial HOXA genes demarcate haematopoietic stem cell fate during human development. *Nat. Cell Biol.* **18**, 595–606 (2016).
- Lee, Y. et al. FGF signalling specifies haematopoietic stem cells through its regulation of somitic Notch signalling. *Nat. Commun.* **5**, 5583 (2014).
- Wilkinson, R. N. et al. Hedgehog and Bmp polarize hematopoietic stem cell emergence in the zebrafish dorsal aorta. *Dev. Cell* **16**, 909–916 (2009).
- Leung, A. et al. Uncoupling VEGFA functions in arteriogenesis and hematopoietic stem cell specification. *Dev. Cell* **24**, 144–158 (2013).
- North, T. E. et al. Runx1 expression marks long-term repopulating hematopoietic stem cells in the midgestation mouse embryo. *Immunity* **16**, 661–672 (2002).
- Tsai, F. Y. et al. An early haematopoietic defect in mice lacking the transcription factor GATA-2. *Nature* **371**, 221–226 (1994).
- Gao, X. et al. Gata2 cis-element is required for hematopoietic stem cell generation in the mammalian embryo. *J. Exp. Med.* **210**, 2833–2842 (2013).
- Butko, E. et al. Gata2b is a restricted early regulator of hemogenic endothelium in the zebrafish embryo. *Development* **142**, 1050–1061 (2015).
- Thambyrajah, R. et al. GF11 proteins orchestrate the emergence of haematopoietic stem cells through recruitment of LSD1. *Nat. Cell Biol.* **18**, 21–32 (2016).
- Zaidan, N. et al. Endothelial-specific Gata3 expression is required for hematopoietic stem cell generation. *Stem Cell Rep.* **17**, 1788–1798 (2022).
- Coulombe, P. et al. Meis1 establishes the pre-hemogenic endothelial state prior to Runx1 expression. *Nat. Commun.* **14**, 4537 (2023).
- Sawamiphak, S., Kontarakis, Z. & Stainier, D. Y. Interferon gamma signaling positively regulates hematopoietic stem cell emergence. *Dev. Cell* **31**, 640–653 (2014).
- Li, Y. et al. Inflammatory signaling regulates embryonic hematopoietic stem and progenitor cell production. *Genes Dev.* **28**, 2597–2612 (2014).
- He, Q. et al. Inflammatory signaling regulates hematopoietic stem and progenitor cell emergence in vertebrates. *Blood* **125**, 1098–1106 (2015).
- Espin-Palazon, R. et al. Proinflammatory signaling regulates hematopoietic stem cell emergence. *Cell* **159**, 1070–1085 (2014).
- Piau, O. et al. Generation of transgene-free hematopoietic stem cells from human induced pluripotent stem cells. *cell Stem cell* **30**, 1610–1623.e1617 (2023).
- Taoudi, S. et al. Extensive hematopoietic stem cell generation in the AGM region via maturation of VE-cadherin+CD45+ pre-definitive HSCs. *Cell Stem Cell* **3**, 99–108 (2008).
- Rybtsov, S. et al. Hierarchical organization and early hematopoietic specification of the developing HSC lineage in the AGM region. *J. Exp. Med.* **208**, 1305–1315 (2011).
- Medvinsky, A. & Dzierzak, E. Definitive hematopoiesis is autonomously initiated by the AGM region. *Cell* **86**, 897–906 (1996).
- de Bruijn, M. F., Speck, N. A., Peeters, M. C. & Dzierzak, E. Definitive hematopoietic stem cells first develop within the major arterial regions of the mouse embryo. *EMBO J.* **19**, 2465–2474 (2000).
- Rybtsov, S. et al. Tracing the origin of the HSC hierarchy reveals an SCF-dependent, IL-3-independent CD43(-) embryonic precursor. *Stem Cell Rep.* **3**, 489–501 (2014).
- Ivanovs, A. et al. Human haematopoietic stem cell development: from the embryo to the dish. *Development* **144**, 2323–2337 (2017).
- Ottersbach, K. Endothelial-to-haematopoietic transition: an update on the process of making blood. *Biochem. Soc. Trans.* **47**, 591–601 (2019).
- Muller, A. M., Medvinsky, A., Strouboulis, J., Grosveld, F. & Dzierzak, E. Development of hematopoietic stem cell activity in the mouse embryo. *Immunity* **1**, 291–301 (1994).
- Bertrand, J. Y. et al. Haematopoietic stem cells derive directly from aortic endothelium during development. *Nature* **464**, 108–111 (2010).



36. Kissa, K. & Herbomel, P. Blood stem cells emerge from aortic endothelium by a novel type of cell transition. *Nature* **464**, 112–115 (2010).
37. Bonkhofer, F. et al. Blood stem cell-forming haemogenic endothelium in zebrafish derives from arterial endothelium. *Nat. Commun.* **10**, 3577 (2019).
38. Furuta, C. et al. Discordant developmental waves of angioblasts and hemangioblasts in the early gastrulating mouse embryo. *Development* **133**, 2771–2779 (2006).
39. Park, C., Kim, T. M. & Malik, A. B. Transcriptional regulation of endothelial cell and vascular development. *Circ. Res.* **112**, 1380–1400 (2013).
40. Cheng, X. et al. Nod1-dependent NF- $\kappa$ B activation initiates hematopoietic stem cell specification in response to small Rho GTPases. *Nat. Commun.* **14**, 7668 (2023).
41. Frame, J. M., Lim, S. E. & North, T. E. Hematopoietic stem cell development: using the zebrafish to identify extrinsic and intrinsic mechanisms regulating hematopoiesis. *Methods Cell Biol.* **138**, 165–192 (2017).
42. Frame, J. M. et al. Metabolic regulation of inflammasome activity controls embryonic hematopoietic stem and progenitor cell production. *Dev. Cell* **55**, 133–149.e136 (2020).
43. Espin-Palazon, R., Weijts, B., Mulero, V. & Traver, D. Proinflammatory signals as fuel for the fire of hematopoietic stem cell emergence. *Trends Cell Biol.* **28**, 58–66 (2018).
44. Lefkopoulos, S. et al. Repetitive elements trigger RIG-I-like receptor signaling that regulates the emergence of hematopoietic stem and progenitor cells. *Immunity* **53**, 934–951.e939 (2020).
45. Kanther, M. et al. Microbial colonization induces dynamic temporal and spatial patterns of NF- $\kappa$ B activation in the zebrafish digestive tract. *Gastroenterology* **141**, 197–207 (2011).
46. Clements, W. K. & Traver, D. Signalling pathways that control vertebrate haematopoietic stem cell specification. *Nat. Rev. Immunol.* **13**, 336–348 (2013).
47. Nash, K. L. & Lever, A. M. Green fluorescent protein: green cells do not always indicate gene expression. *Gene Ther.* **11**, 882–883 (2004).
48. Molina, G. A., Watkins, S. C. & Tsang, M. Generation of FGF reporter transgenic zebrafish and their utility in chemical screens. *BMC Dev. Biol.* **7**, 62 (2007).
49. Natarajan, K., Singh, S., Burke, T. R. Jr., Grunberger, D. & Aggarwal, B. B. Caffeic acid phenethyl ester is a potent and specific inhibitor of activation of nuclear transcription factor NF- $\kappa$ B. *Proc. Natl Acad. Sci. USA* **93**, 9090–9095 (1996).
50. Boisset, J. C. et al. In vivo imaging of haematopoietic cells emerging from the mouse aortic endothelium. *Nature* **464**, 116–120 (2010).
51. Nosedá, M. & Karsan, A. Notch and minichromosome maintenance (MCM) proteins: integration of two ancestral pathways in cell cycle control. *Cell Cycle* **5**, 2704–2709 (2006).
52. Amin, A. et al. An essential and cell-cycle-dependent ORC dimerization cycle regulates eukaryotic chromosomal DNA replication. *Cell Rep.* **30**, 3323–3338.e3326 (2020).
53. Petojevic, T. et al. Cdc45 (cell division cycle protein 45) guards the gate of the eukaryote replisome helicase stabilizing leading strand engagement. *Proc. Natl Acad. Sci. USA* **112**, E249–E258 (2015).
54. Borgstahl, G. E. et al. Interplay of DNA damage and cell cycle signaling at the level of human replication protein A. *DNA Repair* **21**, 12–23 (2014).
55. Kim, J. & MacNeill, S. A. Genome stability: a new member of the RFC family. *Curr. Biol.* **13**, R873–R875 (2003).
56. Roche, B., Arcangioli, B. & Martienssen, R. A. RNA interference is essential for cellular quiescence. *Science* **354**, aah5651 (2016).
57. White, R. J. Transcription by RNA polymerase III: more complex than we thought. *Nat. Rev. Genet.* **12**, 459–463 (2011).
58. Lenardo, M., Pierce, J. W. & Baltimore, D. Protein-binding sites in Ig gene enhancers determine transcriptional activity and inducibility. *Science* **236**, 1573–1577 (1987).
59. Sen, R. & Baltimore, D. Multiple nuclear factors interact with the immunoglobulin enhancer sequences. *Cell* **46**, 705–716 (1986).
60. Espin-Palazon, R. & Traver, D. The NF- $\kappa$ B family: Key players during embryonic development and HSC emergence. *Exp. Hematol.* **44**, 519–527 (2016).
61. Burns, C. E., Traver, D., Mayhall, E., Shepard, J. L. & Zon, L. I. Hematopoietic stem cell fate is established by the Notch-Runx pathway. *Genes Dev.* **19**, 2331–2342 (2005).
62. Liu, F. et al. Cre/lox regulated conditional rescue and inactivation with zebrafish UFlip alleles generated by CRISPR-Cas9 targeted integration. *eLife* **11**, e71478 (2022).
63. Welker, J. M. et al. GeneWeld: efficient targeted integration directed by short homology in zebrafish. *Bio Protoc.* **11**, e4100 (2021).
64. Wierson, W. A. et al. Efficient targeted integration directed by short homology in zebrafish and mammalian cells. *eLife* **9**, e53968 (2020).
65. Thompson, M. A. et al. The cloche and spadetail genes differentially affect hematopoiesis and vasculogenesis. *Dev. Biol.* **197**, 248–269 (1998).
66. Barakat, R., Campbell, C. A. & Espin-Palazon, R. Identification of transcription factor binding sites by cleavage under target and release using nuclease in zebrafish. *Zebrafish* **19**, 104–108 (2022).
67. Hoesel, B. & Schmid, J. A. The complexity of NF- $\kappa$ B signaling in inflammation and cancer. *Mol. Cancer* **12**, 86 (2013).
68. Stachura, D. L. & Traver, D. Cellular dissection of zebrafish hematopoiesis. *Methods Cell Biol.* **101**, 75–110 (2011).
69. Bertrand, J. Y. et al. Definitive hematopoiesis initiates through a committed erythromyeloid progenitor in the zebrafish embryo. *Development* **134**, 4147–4156 (2007).
70. Ciau-Uitz, A., Monteiro, R., Kirmizitas, A. & Patient, R. Developmental hematopoiesis: ontogeny, genetic programming and conservation. *Exp. Hematol.* **42**, 669–683 (2014).
71. Davidson, A. J. & Zon, L. I. The ‘definitive’ (and ‘primitive’) guide to zebrafish hematopoiesis. *Oncogene* **23**, 7233–7246 (2004).
72. Vaughan, S. & Jat, P. S. Deciphering the role of nuclear factor- $\kappa$ B in cellular senescence. *Aging* **3**, 913–919 (2011).
73. Ahn, K. S. & Aggarwal, B. B. Transcription factor NF- $\kappa$ B: a sensor for smoke and stress signals. *Ann. N. Y. Acad. Sci.* **1056**, 218–233 (2005).
74. Scarfo, R. et al. CD32 captures committed haemogenic endothelial cells during human embryonic development. *Nat. Cell Biol.* **26**, 719–730 (2024).
75. Fidanza, A. et al. Single-cell analyses and machine learning define hematopoietic progenitor and HSC-like cells derived from human PSCs. *Blood* **136**, 2893–2904 (2020).
76. Sethi, G., Sung, B. & Aggarwal, B. B. Nuclear factor- $\kappa$ B activation: from bench to bedside. *Exp. Biol. Med.* **233**, 21–31 (2008).
77. Sturgeon, C. M., Ditadi, A., Awong, G., Kennedy, M. & Keller, G. Wnt signaling controls the specification of definitive and primitive hematopoiesis from human pluripotent stem cells. *Nat. Biotechnol.* **32**, 554–561 (2014).
78. Ditadi, A. et al. Human definitive haemogenic endothelium and arterial vascular endothelium represent distinct lineages. *Nat. Cell Biol.* **17**, 580–591 (2015).
79. Kennedy, M. et al. T lymphocyte potential marks the emergence of definitive hematopoietic progenitors in human pluripotent stem cell differentiation cultures. *Cell Rep.* **2**, 1722–1735 (2012).
80. Perala, N. et al. Conservation, expression, and knockdown of zebrafish plxnb2a and plxnb2b. *Dev. Dyn.* **239**, 2722–2734 (2010).

81. Li, X. et al. Generation of destabilized green fluorescent protein as a transcription reporter. *J. Biol. Chem.* **273**, 34970–34975 (1998).
82. Voon, D. C. et al. Use of mRNA- and protein-destabilizing elements to develop a highly responsive reporter system. *Nucleic Acids Res.* **33**, e27 (2005).
83. Kim, A. D. et al. Discrete Notch signaling requirements in the specification of hematopoietic stem cells. *EMBO J.* **33**, 2363–2373 (2014).
84. Shimizu, N., Kawakami, K. & Ishitani, T. Visualization and exploration of Tcf/Lef function using a highly responsive Wnt/beta-catenin signaling-reporter transgenic zebrafish. *Dev. Biol.* **370**, 71–85 (2012).
85. Dorsky, R. I., Sheldahl, L. C. & Moon, R. T. A transgenic Lef1/beta-catenin-dependent reporter is expressed in spatially restricted domains throughout zebrafish development. *Dev. Biol.* **241**, 229–237 (2002).
86. Boisset, J. C. et al. Progressive maturation toward hematopoietic stem cells in the mouse embryo aorta. *Blood* **125**, 465–469 (2015).
87. Li, S. et al. NF-kappaB p65 promotes ovarian cancer cell proliferation and migration via regulating mortalin. *J. Cell. Mol. Med.* **23**, 4338–4348 (2019).
88. Li, D. et al. Myeloid cell RelA/p65 promotes lung cancer proliferation through Wnt/beta-catenin signaling in murine and human tumor cells. *Oncogene* **33**, 1239–1248 (2014).
89. Liu, T., Zhang, L., Joo, D. & Sun, S. C. NF-kappaB signaling in inflammation. *Signal Transduct. Target Ther.* **2**, 17023 (2017).
90. Thambyrajah, R. et al. IkappaBalpha controls dormancy in hematopoietic stem cells via retinoic acid during embryonic development. *Nat. Commun.* **15**, 4673 (2024).
91. Hayden, M. S. & Ghosh, S. Shared principles in NF-kappaB signaling. *Cell* **132**, 344–362 (2008).
92. Sun, S. C. The non-canonical NF-kappaB pathway in immunity and inflammation. *Nat. Rev. Immunol.* **17**, 545–558 (2017).
93. Oeckinghaus, A. & Ghosh, S. The NF-kappaB family of transcription factors and its regulation. *Cold Spring Harb. Perspect. Biol.* **1**, a000034 (2009).
94. Heim, V. J., Stafford, C. A. & Nachbur, U. NOD signaling and cell death. *Front. Cell Dev. Biol.* **7**, 208 (2019).
95. Stein, S. J. & Baldwin, A. S. Deletion of the NF-kappaB subunit p65/RelA in the hematopoietic compartment leads to defects in hematopoietic stem cell function. *Blood* **121**, 5015–5024 (2013).
96. Chen, F. E., Huang, D. B., Chen, Y. Q. & Ghosh, G. Crystal structure of p50/p65 heterodimer of transcription factor NF-kappaB bound to DNA. *Nature* **391**, 410–413 (1998).
97. Rahman, S. M. T. et al. Double knockin mice show NF-kappaB trajectories in immune signaling and aging. *Cell Rep.* **41**, 111682 (2022).
98. Nelson, D. E. et al. Oscillations in NF-kappaB signaling control the dynamics of gene expression. *Science* **306**, 704–708 (2004).
99. Burstyn-Cohen, T. & Kalcheim, C. Association between the cell cycle and neural crest delamination through specific regulation of G1/S transition. *Dev. Cell* **3**, 383–395 (2002).
100. Kohrman, A. Q. & Matus, D. Q. Divide or conquer: cell cycle regulation of invasive behavior. *Trends Cell Biol.* **27**, 12–25 (2017).
101. Ema, H. & Nakauchi, H. Expansion of hematopoietic stem cells in the developing liver of a mouse embryo. *Blood* **95**, 2284–2288 (2000).
102. Ganuza, M. et al. Murine foetal liver supports limited detectable expansion of life-long haematopoietic progenitors. *Nat. Cell Biol.* **24**, 1475–1486 (2022).
103. American Psychological, A. Guidelines for ethical conduct in the care and use of animals. *J. Exp. Anal. Behav.* **45**, 127–132 (1986).
104. Percie du Sert, N. et al. The ARRIVE guidelines 2.0: Updated guidelines for reporting animal research. *PLoS Biol.* **18**, e3000410 (2020).
105. Westerfield, M. *The Zebrafish Book. A Guide for the Laboratory Use of Zebrafish Danio\* (Brachydanio) rerio* (University of Oregon Press, 2000).
106. Lin, H. F. et al. Analysis of thrombocyte development in CD41-GFP transgenic zebrafish. *Blood* **106**, 3803–3810 (2005).
107. Zhu, H. et al. Regulation of the lmo2 promoter during hematopoietic and vascular development in zebrafish. *Dev. Biol.* **281**, 256–269 (2005).
108. Traver, D. et al. Transplantation and in vivo imaging of multilineage engraftment in zebrafish bloodless mutants. *Nat. Immunol.* **4**, 1238–1246 (2003).
109. Correa, R. G. et al. Characterization of NF-kappa B/I kappa B proteins in zebra fish and their involvement in notochord development. *Mol. Cell Biol.* **24**, 5257–5268 (2004).
110. Balciuniene, J. et al. Efficient disruption of Zebrafish genes using a Gal4-containing gene trap. *BMC Genom.* **14**, 619 (2013).
111. Xie, X. et al. Silencer-delimited transgenesis: NRSE/RE1 sequences promote neural-specific transgene expression in a NRSF/REST-dependent manner. *BMC Biol.* **10**, 93 (2012).
112. Jao, L. E., Wentz, S. R. & Chen, W. Efficient multiplex biallelic zebrafish genome editing using a CRISPR nuclease system. *Proc. Natl Acad. Sci. USA* **110**, 13904–13909 (2013).
113. Espin, R. et al. TNF receptors regulate vascular homeostasis in zebrafish through a caspase-8, caspase-2 and P53 apoptotic program that bypasses caspase-3. *Dis. Model Mech.* **6**, 383–396 (2013).
114. Dobin, A. et al. STAR: ultrafast universal RNA-seq aligner. *Bioinformatics* **29**, 15–21 (2013).
115. Putri, G. H., Anders, S., Pyl, P. T., Pimanda, J. E. & Zanini, F. Analysing high-throughput sequencing data in Python with HTSeq 2.0. *Bioinformatics* **38**, 2943–2945 (2022).
116. Love, M. I., Huber, W. & Anders, S. Moderated estimation of fold change and dispersion for RNA-seq data with DESeq2. *Genome Biol.* **15**, 550 (2014).
117. Wang, L., Wang, S. & Li, W. RSeQC: quality control of RNA-seq experiments. *Bioinformatics* **28**, 2184–2185 (2012).
118. Campbell, C. A. et al. A zebrafish model of granulin deficiency reveals essential roles in myeloid cell differentiation. *Blood Adv.* **5**, 796–811 (2021).
119. Zhao, C. et al. Regenerative failure of intrahepatic biliary cells in Alagille syndrome rescued by elevated Jagged/Notch/Sox9 signaling. *Proc. Natl Acad. Sci. USA* **119**, e2201097119 (2022).
120. Thisse, C. & Thisse, B. High-resolution in situ hybridization to whole-mount zebrafish embryos. *Nat. Protoc.* **3**, 59–69 (2008).
121. Pavani, G. et al. Modeling primitive and definitive erythropoiesis with induced pluripotent stem cells. *Blood Adv.* **8**, 1449–1463 (2024).
122. Sullivan, S. K. et al. High-level transgene expression in induced pluripotent stem cell-derived megakaryocytes: correction of Glanzmann thrombasthenia. *Blood* **123**, 753–757 (2014).

## Acknowledgements

This work was supported by the NIH-NIDDK R01 (R01DK131162), NIH-NIDDK R03 (R03DK125661), NIH-NIDDK K01 award (7K01DK115661), and the Roy J. Carver Charitable Trust (#21-5532) to R.E.-P. NIH R24 OD020166 to M.M. and J.J.E. This work was supported in part by the United States Department of Agriculture (USDA) National Institute of Food and Agriculture (NIFA) Hatch project IOWO3717 to K.S.D. and IOWO5706 and Iowa State University start-up funds to C.C. and R.E.-P. The findings and conclusions in this publication are those of the author(s) and should not be construed to represent any official USDA or US Government determination or policy. We thank John Taylor, Inga Baldus, Amelia Case, and Jessica Tupy for technical assistance and fish husbandry, and the ISU DNA and flow cytometry cores for assistance on RNA sequencing and flow cytometry. The authors are indebted to John Rawls

and Michael Tsang for kindly donating the pNFkB:eGFP and Dusp6:-d2EGFP plasmids, respectively, and to Bart Weijts for discussion of ideas.

### Author contributions

C.A.C., R.C., G.P., R.B., X.C., F.L., E.S., X.P., K.S.D., J.J.E., M.M., P.G., D.L.F., and R.E.-P. designed experiments; C.C., R.C., G.P., R.B., X.C., F.L., E.S., and R.E.-P. performed research; C.C., R.C., G.P., R.B., X.C., F.L., X.P., K.S.D., J.J.E., M.M., P.G., D.L.F., and R.E.-P. analyzed data; X.P. and K.D. analyzed RNA-seq data; and C.C. and R.E.-P. wrote the paper with minor contributions from the remaining authors.

### Competing interests

The authors declare no competing interests.

### Additional information

**Supplementary information** The online version contains supplementary material available at <https://doi.org/10.1038/s41467-024-51922-5>.

**Correspondence** and requests for materials should be addressed to Clyde A. Campbell or Raquel Espin-Palazon.

**Peer review information** *Nature Communications* thanks Anna Bigas, and the other, anonymous, reviewer(s) for their contribution to the peer review of this work. A peer review file is available.

**Reprints and permissions information** is available at <http://www.nature.com/reprints>

**Publisher's note** Springer Nature remains neutral with regard to jurisdictional claims in published maps and institutional affiliations.

**Open Access** This article is licensed under a Creative Commons Attribution-NonCommercial-NoDerivatives 4.0 International License, which permits any non-commercial use, sharing, distribution and reproduction in any medium or format, as long as you give appropriate credit to the original author(s) and the source, provide a link to the Creative Commons licence, and indicate if you modified the licensed material. You do not have permission under this licence to share adapted material derived from this article or parts of it. The images or other third party material in this article are included in the article's Creative Commons licence, unless indicated otherwise in a credit line to the material. If material is not included in the article's Creative Commons licence and your intended use is not permitted by statutory regulation or exceeds the permitted use, you will need to obtain permission directly from the copyright holder. To view a copy of this licence, visit <http://creativecommons.org/licenses/by-nc-nd/4.0/>.

© The Author(s) 2024